CM² MAGAZINE

第 53 期

南方科技大学海洋磁学中心

https://cm2.sustech.edu.cn/

创刊词

海洋是生命的摇篮，是文明的纽带。地球上最早的生命诞生于海洋，海洋里的生命最终进化成了人类，人类的文化融合又通过海洋得以实现。人因海而兴。

人类对海洋的探索从未停止。从远古时代美丽的神话传说，到麦哲伦的全球航行，再到现代对大洋的科学钻探计划，海洋逐渐从人类敬畏崇拜幻想的精神寄托演变成可以开发利用与科学研究的客观存在。其中，上个世纪与太空探索同步发展的大洋科学钻探计划将人类对海洋的认知推向了崭新的纬度：深海（deep sea）与深时（deep time）。大洋钻探计划让人类知道，奔流不息的大海之下，埋藏的却是亿万年的地球历史。它们记录了地球板块的运动，从而使板块构造学说得到证实；它们记录了地球环境的演变，从而让古海洋学方兴未艾。

在探索海洋的悠久历史中，从大航海时代的导航，到大洋钻探计划中不可或缺的磁性地层学，磁学发挥了不可替代的作用。这不是偶然，因为从微观到宏观，磁性是最基本的物理属性之一，可以说，万物皆有磁性。基于课题组的学科背景和对海洋的理解，我们对海洋的探索以磁学为主要手段，海洋磁学中心因此而生。

海洋磁学中心，简称 CM^2，一为其全名“Centre for Marine Magnetism”的缩写，另者恰与爱因斯坦著名的质能方程 $E = MC^2$ 对称，借以表达我们对科学巨匠的敬仰和对科学的不懈追求。

然而科学从来不是单打独斗的产物。我们以磁学为研究海洋的主攻利器，但绝不仅限于磁学。凡与磁学相关的领域均是我们关注的重点。为了跟踪反映国内外地球科学特别是与磁学有关的地球科学领域的最新研究进展，海洋磁学中心特地主办 CM^2 Magazine，以期与各位地球科学工作者相互交流学习、合作共进！

“海洋孕育了生命，联通了世界，促进了发展”。 21 世纪是海洋科学的时代，由陆向海，让我们携手迈进中国海洋科学的黄金时代！

目 录

磁学演绎 1

第 43 章 沉积后磁学信息 1

文献速递 **9**

1. 末次冰期终止期海洋铁施肥效应与 CO_2 下降在区域和空间上的演化 9
2. 古新世-始新世极热事件开启时陆地甲烷循环扰动 13
3. 热化学岩石圈分异与克拉通地幔的起源 15
4. 海底热液循环通道的磁成像 17
5. 来自中欧的新的地磁长期变化数据二：古强度 21
6. 拉萨地块（西藏）从冈瓦纳到欧亚大陆中生代漂移的古地磁约束 23
7. 古菲律宾海板块的特征:来自菲律宾东部海域岩石圈碎片的证据 25
8. 青藏高原季节性升温异常对东亚夏季风降水的先驱影响 28
9. 探索考古地球物理学中收集的数据一致性：来自 Villasviejas del Tamuja（西班牙埃斯特马杜）铁器时代希尔夫特的案例研究 31
10. 不同细菌和培养温度对微生物合成磁铁矿与锰替代磁铁矿纳米颗粒的影响 33
11. 古气候研究在中国考古中的尺度不匹配 35
12. 亚速尔群岛全矢量古长期变化曲线:为过去 2kyr 提供可靠的古地磁测年 37
13. Bølling–Allerød 时期北美中纬度地区广泛的湿地发育 40

磁学演绎

第 43 章 沉积后磁学信号

1. 成土作用与土壤

土壤的形成，即成土过程，是母质在成土因素的综合作用下所经历的一系列物理化学改造的过程[e.g., Vincent et al., 1994]。这里所指的成土因素包括气候、有机质、地形、母质和成土时间[Jenny, 1941; 1980]。自然界中，土壤剖面表现出水平层状构造，称为土壤发生层，反映了土壤形成过程中物质的迁移、转化和累积的特点。A 层（腐殖质层）有机质含量最高，但可溶性组分（例如硅酸盐粘土，铁，铝和腐殖质）会由于淋溶作用在 B 层（淀积层）聚集。而 C 层（母质层）则主要代表了未受改造的土壤母质。以往的研究表明，土壤剖面 A、B 层中，含铁粘土矿物和铁镁质硅酸盐可作为铁源[Spassov et al., 2003]，产生纳米级亚铁磁性矿物 [Zhou et al., 1990; Maher, 1998]，导致磁化率的显著增强 [Maher et al., 1998]。因此，土壤的磁学性质携带了成土过程 [Zhou et al., 1990; Tauxe et al., 1990; Singer et al., 1996] 和磁学性质与气候之间关系的重要信息[Maher et al., 1994]。

通常情况下，风成碎屑物质和土壤母质的磁性较弱且均一，例如亚洲和欧洲的黄土沉积，尤其是中国黄土高原的黄土沉积。然而，在黄土/古土壤序列中，古土壤却因为大量成土磁铁矿/磁赤铁矿的生成而磁性较强[e.g., Kukla et al., 1988; Zhou et al., 1990; Liu et al., 2007a]。迄今为止，关于古土壤中磁赤铁矿的生成机制主要有两种假设：直接析出和作为水铁矿转化的中间产物。直接析出机制实际上是一种发酵作用，有机质和铁还原细菌将三价铁还原为二价铁，形成纳米级磁铁矿，之后再被氧化为磁赤铁矿 [Mullins, 1977]。第二种机制中，弱磁性的水铁矿在添加了吸附配体，如磷酸盐、柠檬酸盐的条件下向赤铁矿转化，转化过程中会生成强磁性的水铁矿中间产物（磁赤铁矿）[Barrón and Torrent, 2002; Barrón et al., 2003; Michel et al., 2010]。事实上，之所以关于成土过程中磁性矿物的转化过程很难有定论，主要是因为转化过程的中间产物很少能够被保存，我们所能观察和测量到的都是最终产物。即使如此，我们仍然能够从土壤中强磁性磁赤铁矿、弱磁性赤铁矿和针铁矿的含量中得到有用的启示。研究表明，土壤中只有赤铁矿和纳米级磁赤铁矿有固有的内在联系 [Ji et al., 2001; Liu et al., 2006b; Lyons et al.,

2010]。Liu et al. [2010] 在西班牙年代序列土壤剖面中，观察到成土成因的磁赤铁矿的解阻温度（与磁性矿物的大小有关）和其含量存在正相关关系。然而，在黄土高原剖面的古土壤中，磁性颗粒的粒径分布统一并存在一个 25 纳米的峰值，且不随成土作用的程度而改变，因此代表了成土过程的第二阶段，即较成熟的阶段 [Liu et al., 2005a, 2007a]。这说明，黄土高原古土壤中成土磁赤铁矿演化为一个成熟的阶段从而显示出颗粒大小的均一性。

虽然成土过程中磁性矿物的形成受到多种因素的控制，例如温度、降水、有机碳含量、pH 值、Eh 值等，但统计分析显示现代土壤的磁学性质，尤其是磁化率大小，主要受控于降水量的多少 [Heller et al., 1993; Maher et al., 1994; Maher and Thompson, 1995; Maher, 1998; Florindo et al., 1999; Maher et al., 2002, 2003; Maher and Hu, 2006; Geiss et al., 2004; Liu et al., 2005c]。这就为重建过去降水量的时间和空间分布提供了可能性 [Maher et al., 1994; Maher and Thompson, 1995]。然而，土壤磁化率和降水量之间的关系是非线性的。当降水量超过一个临界值（~550-600 mm/yr）时，亚铁磁性矿物的含量就会受到溶解作用而降低 [Han et al., 1996; Balsam et al., 2004]。Guo et al. [2001] 和 Bloemendal and Liu [2005] 的研究认为，磁性矿物的形成和气候之间的关系非常复杂。Liu et al. [2007a] 建立一个概念模型，该模型中提出赤铁矿和磁铁矿/磁赤铁矿的含量比值（Hm/Mag）相比磁化率，是更好的评估古降水的指标，因为该参数和降水量的相关关系更加单调 [Torrent et al., 2006]。

Orgeira and Compagnucci [2006] 认为是潜在蓄水量（PWS）而不是总降水量影响了成土过程中磁性矿物的生成。PWS 代表了年降水量的纯盈余，定义为总降水量和总蒸发量的差值。当 PWS 为负时，即降水量支出大于收入（例如在黄土高原和俄罗斯大草原），还原作用被抑制，因此风尘成因的磁性物质被保存，有利于成土过程中纳米级磁性矿物的生成。相反，当 PWS 为正时（例如阿根廷黄土），有利于磁性矿物的溶解。磁学古气候转换公式为半定量评估轨道尺度上和区域尺度上古气候变化提供了有力的工具，但前提是在研究区域中，沉积后磁性矿物的溶解作用影响很小且土壤的母质和磁性矿物含量相对均一[Maher and Thompson, 1995]。

黄土高原和俄罗斯大草原土壤一致表现为磁性的增强；中国黄土/古土壤序

列中磁化率的变化和深海氧同位素的变化显示出明显的正相关，证明了区域气候（如亚洲季风系统）和全球气候在轨道、亚轨道[Liu, 1985; Liu and Ding, 1998]，甚至是千年尺度上的遥相关[Porter and An, 1995; Chen et al., 1997]（图 1）。不仅如此，阿拉伯半岛的粉尘记录和黄土高原的粉尘记录的对比揭示出在过去 5 个冰期循环中，大气循环在轨道、亚轨道和千年尺度上也存在遥相关 [Roberts et al., 2011c]。Chen et al. [1997] 研究了黄土高原西部三个马兰黄土剖面（<75 ka），发现其磁学和非磁学参数的变化和格陵兰以及南极冰芯的气候记录非常相似。Deng et al. [2006] 研究了黄土高原北缘靖边黄土/古土壤序列，发现 2.6 Ma 以来，受到全球变冷及其他因素的影响，亚洲内陆持续干旱化。而 Guo et al. [2002] 证明了中国黄土/古土壤序列可以延伸至约 22 Ma。这就说明从早中新世以来，亚洲内陆的粉尘源区和亚洲冬季风系统就已经存在，而它们的存在很有可能是受到青藏高原持续隆升和全球变冷所导致的干旱化的影响。Oldfield and Bloemendal [2011] 再次证明中国中新世的黄土是风成沉积。Hao et al. [2008] 的研究显示，中新世黄土序列的磁学性质在轨道和亚轨道尺度上变化，但其变化行为要比年轻的风尘序列复杂的多。

样品的磁化率受到多种因素的控制，磁化率绝不仅仅是一个简单的古气候指标[Sun and Liu, 2000; Guo et al., 2001]。除了磁化率外，Banerjee et al. [1993] 用低温磁学技术分离了黄土高原样品所承载的局地和区域古气候信号。无独有偶，Hunt et al. [1995b] 使用多种磁学参数来研究黄土中磁性矿物的含量、组成和粒径。许多研究表明，磁学参数的变化并不能直接与亚洲夏季风的强度相联系[Vidic et al., 2003; Sun et al., 2006a]。不同剖面间磁学信号的时间差异主要是受季风、降水时间和降水量影响。为了更好的理解这个问题，Hao and Guo [2005]建立了 600 ka 以来中国黄土磁化率变化的空间分布图。在这些等值线图中，有许多磁化率低值的聚集点，即所谓的“公牛眼”，它们与局部的地形息息相关。在典型的情况下，亚洲夏季风在黄土高原西部是减弱的。然而，当解释单个剖面在长尺度上的磁学变化时必须格外注意。例如，黄土高原 L8 的磁化率非常低，磁性矿物粒度非常粗。然而，在塔吉克斯坦的黄土剖面中，同样的 L8 磁性矿物粒径却只是平均值水平。这就意味着，黄土高原上 L8 的特征是一个局地的效应，极有可能与粉尘物源区的扩张有关 [Yang et al., 2006]。然而，总体来说，环境磁学

的研究在季风、古降水以及黄土和其他风尘沉积的沉积过程中取得了丰硕的成果。

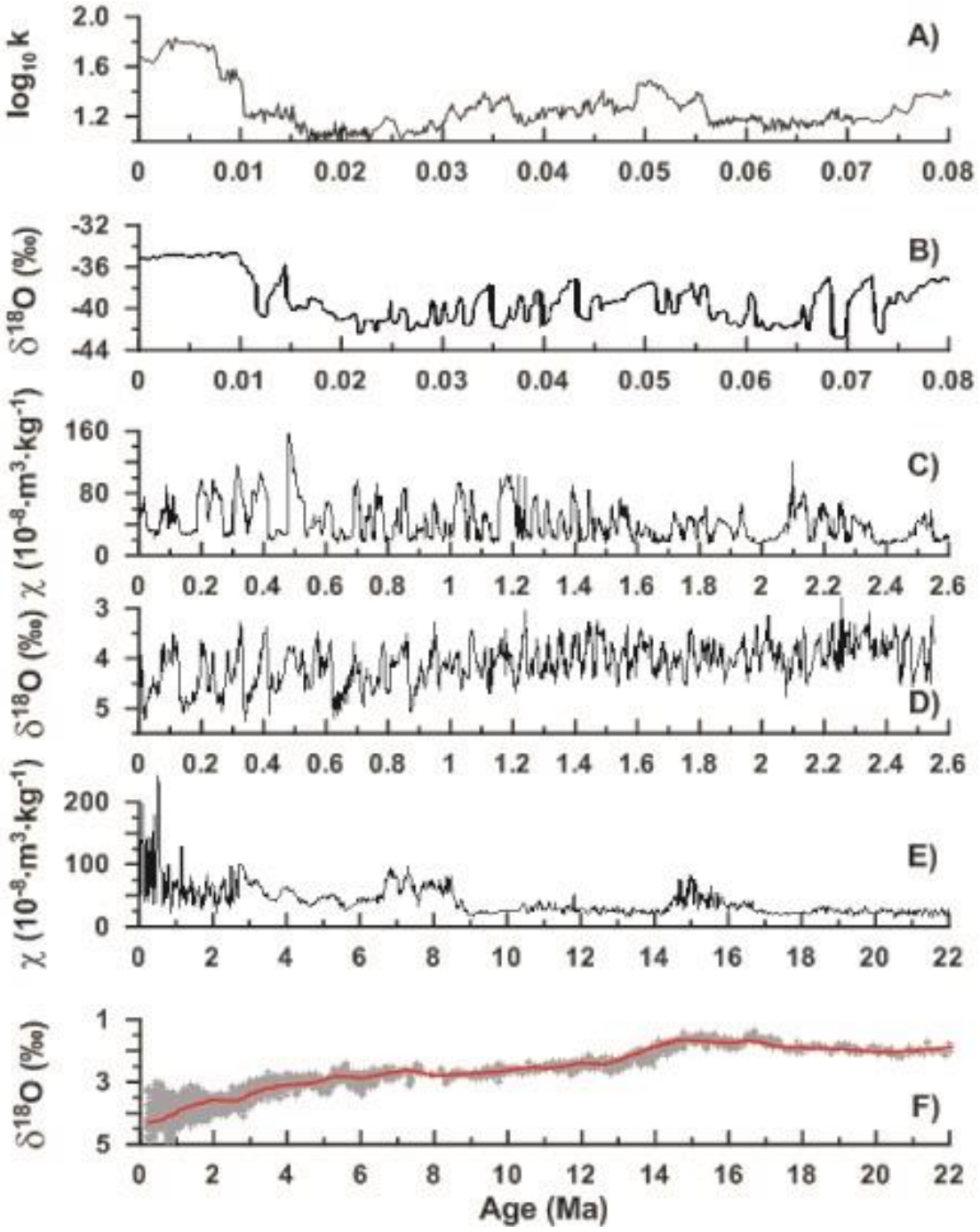

图 1. 不同时间尺度上，中国黄土/古土壤的磁化率与深海氧同位素之间的比较. (A-B) <0.08 Ma；(C-D) < 2.6 Ma； (E-F) < 22 Ma. 其中(A-B)数据来源于 Chen et al. [1997]，(C-D) 数据来源于 Ding et al. [2005]，(E) 数据来源于 Guo et al. [2002]，(F) 数据来源于 Zachos et al. [2001]。

2. 成岩作用

成岩过程中的化学反应也是影响海洋和湖泊沉积物磁学性质的主导因素。成岩作用对沉积物的影响程度取决于有机质的类型和供给以及底层水和沉积物孔隙水的含氧量。陆架和陆坡上的海洋沉积物有大量陆源的输入和有机碳。在这些剖面中，表层沉积物通过与含氧量较高的底层水的接触而被氧化，但下层的沉积物却由于强烈的微生物活动和快速的沉积阻断了氧气的扩散而处于缺氧环境。这就导致了海洋沉积物的分带：上层有氧带，利于保存原始的陆源碎屑磁性矿物；次氧化带，磁铁矿开始被溶解；缺氧带，绝大部分碎屑磁性矿物被溶解。早期的成岩作用伴随有自生胶黄铁矿的生成，首先是在过渡带生成 SP 胶黄铁矿，最终在缺氧的底层带形成 SD 胶黄铁矿[Rey et al., 2000, 2005; Emiroglu et al., 2004; Liu et al., 2004; Roberts and Weaver, 2005; Kawamura et al., 2007; Rowan et al., 2009; Mohamed et al., 2011]。随着沉积的继续，这些条带向上层迁移，通过缺氧带的沉积物最终会形成碎屑磁性矿物被溶解，SP、SD 胶黄铁矿出现的特点。这种情形在浅海沉积 [Rey et al., 2000, 2005; Emiroglu et al., 2004; Liu et al., 2004; Kawamura et al., 2007; Zheng et al., 2010; Mohamed et al., 2011; Roberts et al., 2011a] 和沉积速率较快的深海沉积中非常常见 [e.g., Leslie et al., 1990; Tric et al., 1991; Roberts and Turner, 1993; Florindo and Sagnotti, 1995; Horng et al., 1998; Robinson et al., 2000; Jiang et al., 2001; Roberts and Weaver, 2005; Dillon and Bleil, 2006; Vassiliev et al., 2008; Rowan et al., 2009; Roberts et al., 2011a]，这也是海洋沉积物经历了成岩作用还原后缺乏真正的沉积古地磁信号的原因。

硫酸盐的还原溶解形成过量铁，抑制了黄铁矿化的进行，从而有利于自生胶黄铁矿的保存 [Kao et al., 2004]。铁和硫酸盐的含量以及活动性则受控于动态化学梯度，也与沉积物的母质、有机碳供给的变化有关。因此，胶黄铁矿存在的环境学意义不在于它的含量变化而在于它代表着缺氧的环境。自生胶黄铁矿的生成与陆源供给[Blanchet et al., 2009]以及底层水透气性相关就是很好的例子[Vigliotti, 1997; Larrasoaña et al., 2003b]。然而，尽管还原成岩作用常常改变河流和风成沉积物的陆源信号，但冰和底层水所带来的陆源沉积信号却很少被还原成岩作用所掩盖。很多研究报道了海洋沉积物中还原成岩作用改变了与河流相关的磁性信号，甚至危及到了磁性矿物所携带的古环境信息[Abrajevitch and Kodama, 2011]。然而，当海洋沉积物中有风成粉尘沉积时，还原成岩作用并没有阻碍分离富含赤铁

矿的风成沉积信号，可能是由于研究的沉积环境含氧量较高或者是赤铁矿在还原环境下抗溶解性更好导致的[Bloemendal et al., 1993; Larrasoaña et al., 2003a; Abrajevitch and Kodama, 2011]。硫化物络合作用是驱动还原溶解的最终动力，因此，不同矿物的表面性质对硫化物络合作用的影响可能是海洋沉积物中赤铁矿抗溶解性更强的原因 [Poulton et al., 2004]。此外，同形铝铁替代作用也会降低赤铁矿和针铁矿和硫化物的反应性 [Liu et al., 2004a]。

另外一个产生可溶硫酸盐并促进自生胶黄铁矿生长的过程是甲烷的厌氧氧化作用 [e.g., Housen and Musgrave, 1996; Kasten et al., 1998; Neretin et al., 2004; Garming et al., 2005; Musgrave et al., 2006; Van Dongen et al., 2007; Enkin et al., 2007; Larrasoaña et al., 2007; Fu et al., 2008; Chen et al., 2009; Roberts et al., 2011a]和渗流中烃类的降解 [Reynolds et al., 1991]。当这些过程对沉积物的影响时间较长时（例如持续到成岩作用早期的末端），还会形成单斜磁黄铁矿[Reynolds et al., 1991; Housen and Musgrave, 1996; Musgrave et al., 2006; Larrasoaña et al., 2007; Roberts et al., 2010]。天然气水合物是碳循环中的关键因素，而它们早期形成则是研究的难点。富天然气水合物海洋沉积物中含有成岩作用胶黄铁矿和磁黄铁矿，因此，这些磁性矿物也为古老沉积物中天然气水合物的探测提供了标志[Housen and Musgrave, 1996; Larrasoaña et al., 2007; Van Dongen et al., 2007; Chen et al., 2009; Roberts et al., 2010]。

在那些水深较深（大于 1 km），沉积速率较慢的地区，陆源输入和有机碳含量都会减少。上层有氧层厚度增加，而下层缺氧层减薄，且常出现在沉积物和水交界面以下几十甚至几百米。有时候，由于有机物的缺乏，沉积速率较慢，会导致上层水中的氧向下扩散，从而使得缺氧层缺失。在这种情况下，有可能形成针铁矿和赤铁矿，并且和已存在的磁性矿物共存[Channell et al., 1982; Freeman, 1986; Galbrun et al., 1994; Moreau et al., 1994; Mamet and Preat, 2006]。但这时赤铁矿和针铁矿的环境意义是不确定的，因为它们有可能是在沉积后几千年甚至几百万年的范围内产生的。不过它们的出现还是与沉积物堆积过程中底层水的氧化作用相关。

在慢速堆积的深海沉积物中，氧化环境比较流行，但可以被有机物供给的增加和底层水氧化所突然中断。Tarduno [1994] 认为冰期增加的有机碳供给导致了

沉积层中磁铁矿的还原溶解。不稳定的还原成岩环境和底层水氧化的关系也被东地中海沉积物中广泛出现的磁铁矿还原溶解和胶黄铁矿的自生所证实，原因正是轨道周期控制的腐泥层的降解 [van Santvoort et al., 1997; Roberts et al., 1999; Passier et al., 2001; Kruiver and Passier, 2001; Passier and Dekkers, 2002; Larrasoaña et al., 2003b, 2006]。腐泥层形成后氧气的渗入导致了古氧化边界处自生磁铁矿的生成[Passier et al., 2001; Kruiver and Passier, 2001; Passier and Dekkers, 2002; Larrasoaña et al., 2003b, 2006; Garming et al., 2004]。磁学数据和地化数据的对比显示，腐泥层所指示的还原成岩环境及其导致的磁学特征与增强的有机碳供给和底层水透气作用的减弱息息相关，且底层水透气性减弱是影响磁学性质的最终因素[Larrasoaña et al., 2003b]。全钻孔测量技术的应用，使得长时间尺度沉积物高精度磁学性质的研究成为可能，并成功应用于东地中海长尺度气候调谐的底层水透气性变化的研究中 [Larrasoaña et al., 2003b]。

湖泊沉积物的磁性变化也会受到还原成岩作用的影响。湖泊中的有机质，尤其是生物活动产生的有机质，稀释了物源磁性矿物的含量，导致磁学参数之间的负相关性。此外，物源磁性矿物在有机碳丰富，缺氧的还原成岩环境下的淡水沉积物中部分或者全部溶解，其机制与海洋沉积物中相似，都是以微生物活动为媒介[e.g., Berner, 1980; Snowball and Thompson, 1988, 1990; Roberts et al., 1996; Williamson et al., 1998; Reynolds et al., 1999]。这种还原环境受控于湖水高度，沉积速率、有机碳含量、铁和硫化物的可用性 [Berner, 1984]、含铁矿物的粒度和组成 [Hilton and Lishman, 1985; Anderson and Rippey, 1988; Canfield et al., 1992; Morse and Wang, 1997; Poulton et al., 2004]。例如，湖面高度和层理强烈影响湖泊的沉积环境和磁性矿物的保存。Williamson et al. [1998] 研究了马达加斯加热带玛珥湖的沉积物。其中，高矫顽力的氧化物在湖面水位较低的干旱时期被保存，而在湖水稳定，分层时期的薄层富菱铁矿沉积物中缺失。在硫化/非硫化环境下，自生菱铁矿可以形成并与胶黄铁矿和黄铁矿在硫化环境中共存[Berner, 1980; Oldfield et al., 1992; Roberts and Weaver, 2005]。这时，全样磁化强度的增强或者减弱取决于最终产物是胶黄铁矿还是非亚铁磁性矿物。Stockhausen and Thouveny [1999] 研究了末次冰消期法国 Lac du Bouchet 湖及其相邻两个玛珥湖沉积物的磁学性质。研究发现，即使是可以很好代表古气候变化的 Lac du Bouchet 湖磁化

率记录也因为沉积后磁铁矿的溶解而部分减弱。三个湖之间磁化率记录的弱相关证明了局地因素（溶解和稀释）对原始气候调谐的物源记录的影响。

文献速递

1. 末次冰期终止期海洋铁施肥效应与 CO_2 下降在区域和空间上的演化

翻译人：仲义 zhongy@sustech.edu.cn

Fabrice Lambert, Natalia Opazo, Andy Ridgwell., et al., ***Regional patterns and temporal evolution of ocean iron fertilization and CO_2 drawdown during the last glacial termination*** *[J]* ***Earth and Planetary Science Letters****, 2020, 554, 116675.*
https://doi.org/10.1016/j.epsl.2020.116675

摘要：上一次的地球气候急剧变暖与上一次冰期的结束有关，当时大气的二氧化碳浓度从末次冰期（LGM,26-19 ka）的 180 ppmv 上升至全新世早期的最大值（12-8 kaBP）。大约 1/4 的差异被认为是由于冰川时期更强的生物泵作用造成的，这是由风尘的增加搜驱动的，因此海洋表层水中铁含量更高。然而，在冰川消融过渡时期，沙尘供应并没有均匀地或同步地变化，而我们也无法了解不同海洋区域的相对重要性及其他们是如何随着时间发生变化的。作者利用一个中等复杂性的地球系统模型，我们量化了大气二氧化碳对区域铁供应变化的敏感性，并测试了六种不同的全球粉尘重建，来探索过去粉尘变化。结果显示南大洋（>34° S）是铁施肥效应最敏感的区域，而大西洋和太平洋组分别占全球铁施肥导致 CO2 总体下降的 41±23%和 16±10%左右。然而，北太平洋贡献了北半球对于驱动冰消期 CO2 升高的 28±3%。除此之外，我们的分析揭示了意想不到的空间与时间的差异性，虽然南半球的铁施肥对大气的二氧化碳的影响在整个终止过程中相对持续，而北半球的影响只发生在终止期的后期。

ABSTRACT: The last time Earth's climate experienced geologically rapid global warming was associated with the last glacial termination, when atmospheric CO2 concentrations rose from 180 ppmv during the Last Glacial Maximum (LGM, 26-19 kaBP) to ~260 ppmv by the early Holocene (12-8 kaBP). About one quarter of that difference is thought to be due to a stronger biological pump during glacial times, driven by increased aeolian dust deposition and hence greater iron availability in ocean surface waters. However, dust supply did not change uniformly or in synchrony over the deglacial transition and what is not known is the relative importance of different oceanic regions

and how this may have changed in time. Using an Earth system model of intermediate complexity, we quantify the sensitivity of atmospheric CO2 to regional changes in iron supply, and test six different global dust reconstructions in order to explore uncertainty in past dust changes. We confirm the Southern Ocean (>34◦S) as the region most sensitive to iron fertilization, with the Atlantic and Pacific sectors accounting for about 41±23% and 16±10%, respectively, of the total CO2 reduction from global iron fertilization. However, the North Pacific contributes 28±3% to the total implying an important role for Northern Hemisphere processes in driving deglacial CO2 rise. In addition, our analysis reveals an unexpected regional-temporal disparity, and while Southern Hemisphere iron fertilization influences atmospheric CO2 relatively constantly throughout the termination the impact of the Northern Hemisphere only occurs during the later stages of the termination.

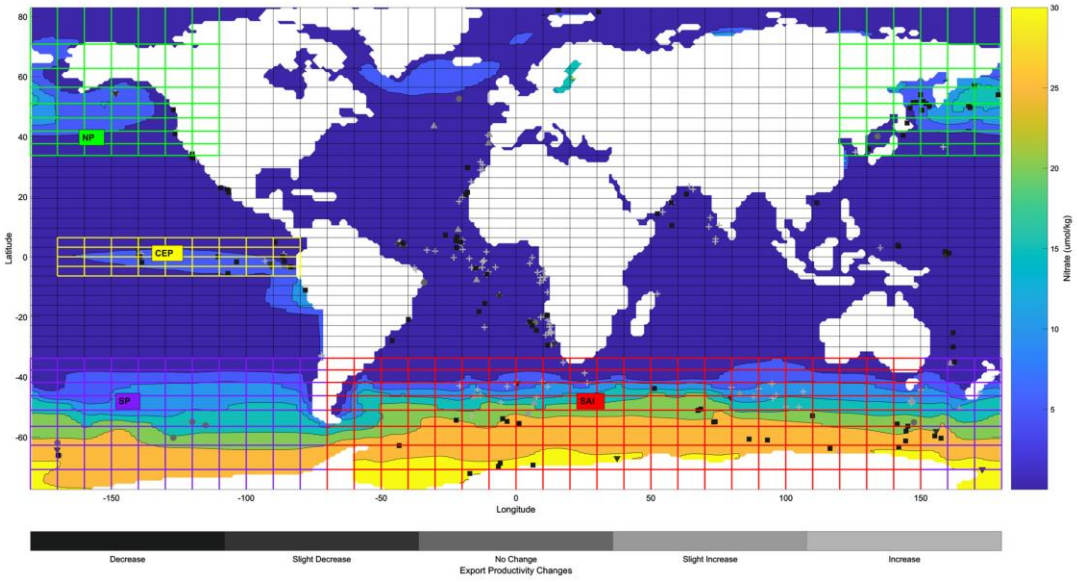

Figure 1. World grid as used as input for the cGENIE model. Ocean color represents Holocene nitrate surface concentrations (Lambert et al., 2015) (right colorbar). The 4 main HNLC regions (SAI, SP, NP, CEP) are marked in color. The plus signs, upward-pointing triangles, circles, downward-pointing triangles, and squares represent LGM-Holocene export productivity increase, slight increase, no change, slight decrease, and decrease, respectively, measured in marine sediment cores (Kohfeld et al., 2013, 2005; Kohfeld and Chase, 2011) and color-coded in the bottom color bar (Albani et al., 2014; Lambert et al., 2015; Ohgaito et al., 2018; Sueyoshi et al., 2013; Takemura et al., 2009; Yukimoto et al., 2012). (For interpretation of the colors in the figure(s), the reader is referred to the web version of this article.)

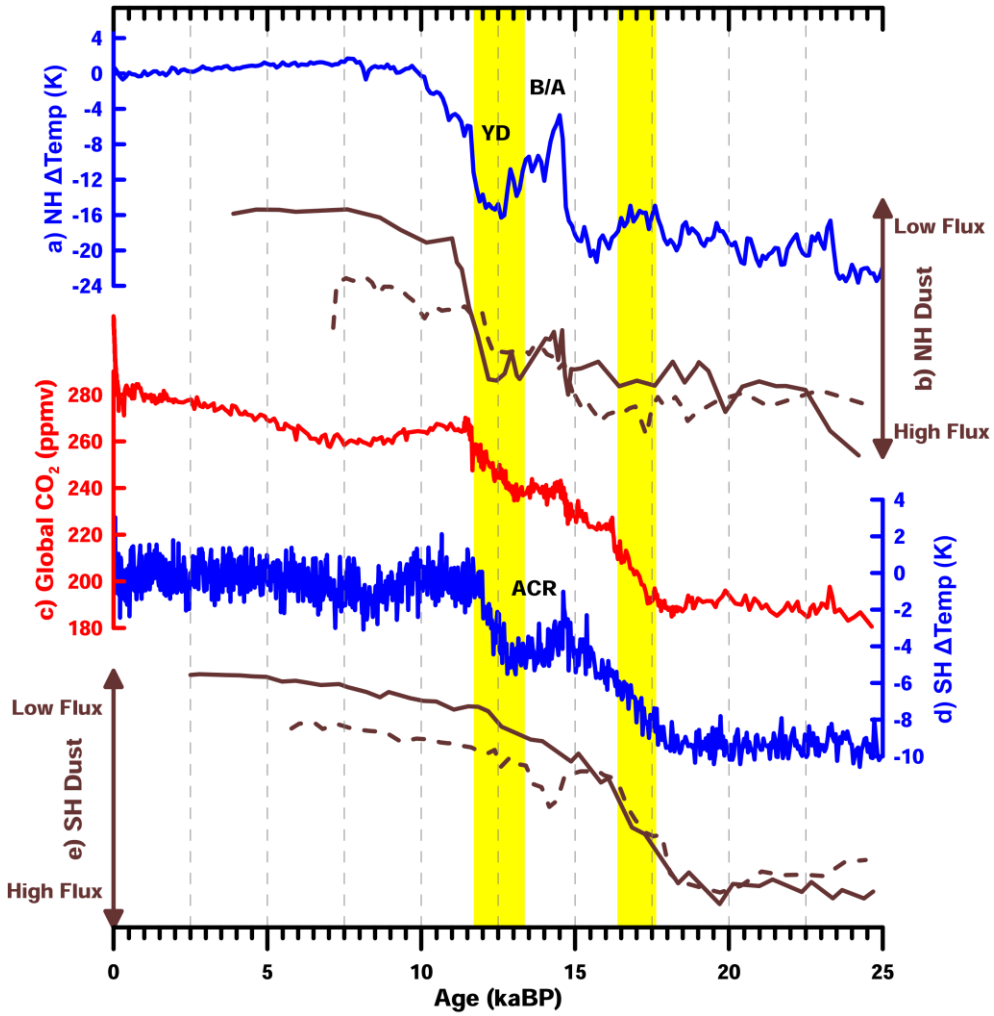

Figure 2. a) Greenland ice-core temperature fluctuations (Masson-Delmotte et al., 2006). b) Aeolian dust deposition in the North Pacific (Serno et al., 2014) (full line) and the Equatorial Pacific (Jacobel et al., 2016) (dotted line). c) Global CO2 concentrations from an Antarctic ice-core (Bereiter et al., 2015). d) Antarctic ice-core temperature fluctuations (Jouzel et al., 2007). e) Aeolian dust deposition in the South Atlantic (Anderson et al., 2014) (full line) and the South Pacific (Lamy et al., 2014) (dotted line).

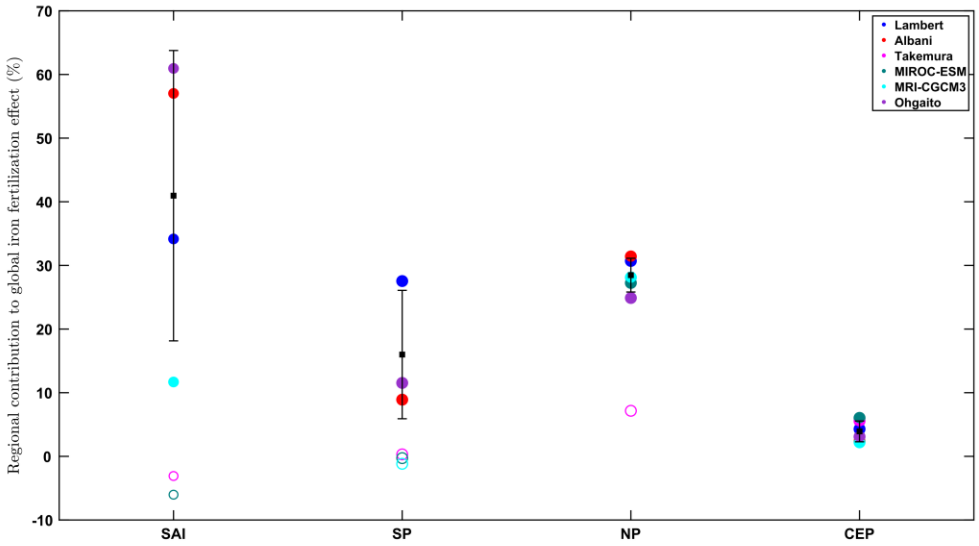

Figure 3. Relative contribution of each HNLC region (South Atlantic and Indian, South Pacific, North Pacific, Central Eastern Pacific) to the atmospheric CO2 changes in the global simulation for each dust dataset. Empty circles in SAI and SP were excluded due to missing representation of Patagonian and Oceanian glaciogenic emissions in these LGM simulations. The black square with error bars shows the mean and standard deviation of the not excluded results.

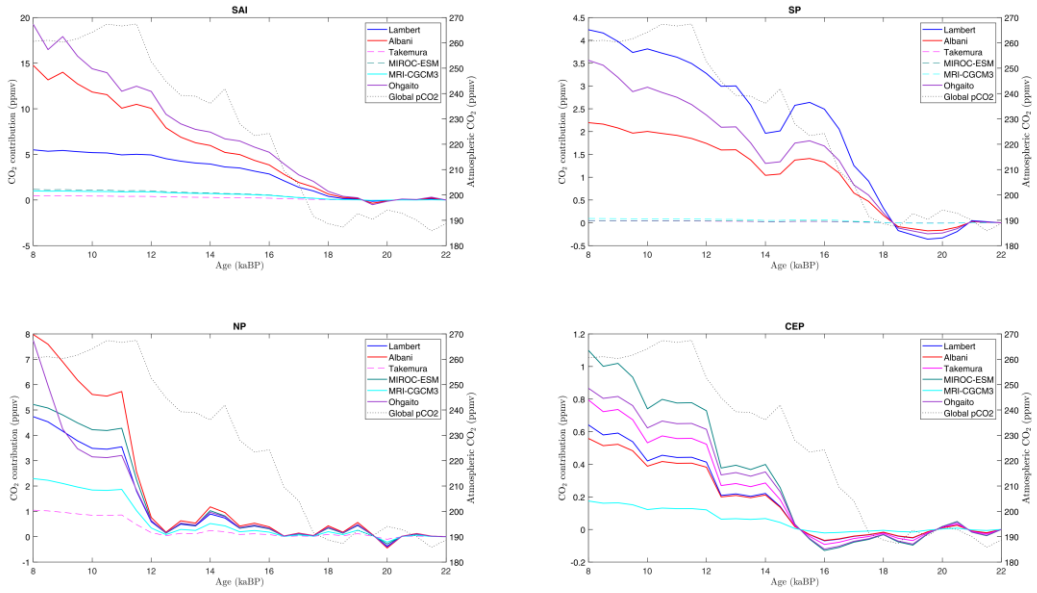

Figure 4. The colored lines show the calculation of the CO2 response to dust deposition based on the mathematical formula derived in Figure S5 and applied to the scaled measured dust flux time series in each HNLC region. Dashed lines in SAI, SP, and NP show the excluded results from Fig. 4. The global atmospheric CO2 record is shown as a black dotted line plotted against the right axis.

2. 古新世-始新世极热事件开启时陆地甲烷循环扰动

翻译人：蒋晓东 jiangxd@sustech.edu.cn

Inglis G N, Rohrssen M, Kennedy E M, et al. ***Terrestrial methane cycle perturbations during the onset of the Paleocene-Eocene Thermal Maximum*** *[J]. Geology, 2020.*

https://doi.org/10.1130/G48110.1

摘要：在古新世-始新世极热时期（PETM；56 Ma）陆地甲烷释放可能已经增强，并且促进了额外的暖效应尤其在高纬度地区。尽管有证据表明在北半球区域甲烷循环增强，然而该现象是否在全球区域广泛存在仍然未知，因为缺乏温度变化与甲烷循环之间的比较。本项目使用生物标志物在新西兰 PETM 剖面重建了温度变化和甲烷循环。结果显示基于细菌霍烷的碳同位素（$\delta^{13}C$）在 PETM 初始时降至极低值（-60‰），这表明增强的甲烷消耗。这远低于现今湿地碳同位素值，表明 PETM 初始时具有显著的甲烷扰动。不管高温证据，低霍烷碳同位素并未持续至早始新世时期，这表明在短暂的与逐渐暖化的事件比较时陆地甲烷显著不同。在 PETM 时期增强的甲烷循环可能有助于解决高纬度地区温度数据模型的不匹配，可以解释更高估算的地球系统敏感性相较仅基于二氧化碳的估算。

ABSTRACT: Terrestrial methane (CH_4) emissions may have increased during the Paleocene-Eocene Thermal Maximum (PETM; ca. 56 Ma) and promoted additional warming, especially in the high latitudes. Although there is evidence for increased CH_4 cycling in a single Northern Hemisphere site, whether enhanced methane cycling was globally widespread is unknown because there have been no subsequent investigations. The mechanism of CH_4 release is also unknown because a direct comparison between temperature and CH_4 cycling has so far not been possible. Here we use biomarkers to reconstruct temperature change and CH_4 cycling in a new PETM-aged succession in New Zealand. Our results indicate that the stable carbon isotopic composition ($\delta^{13}C$) of bacterial hopanoids decreased to very low values (−60‰) during the onset of the PETM, indicating enhanced consumption of CH_4. These values are much lower than found in modern wetlands and suggest a major perturbation of the CH_4 cycle during the onset of the PETM. Low

hopanoid $\delta^{13}C$ values do not persist into the early Eocene, despite evidence for elevated temperatures. This indicates that the terrestrial CH_4 cycle operates differently during transient compared to gradual warming events. Enhanced CH_4 cycling during the PETM may help to resolve the temperature data-model mismatch in the high latitudes and could yield higher estimates of Earth system sensitivity than expected from CO_2 alone.

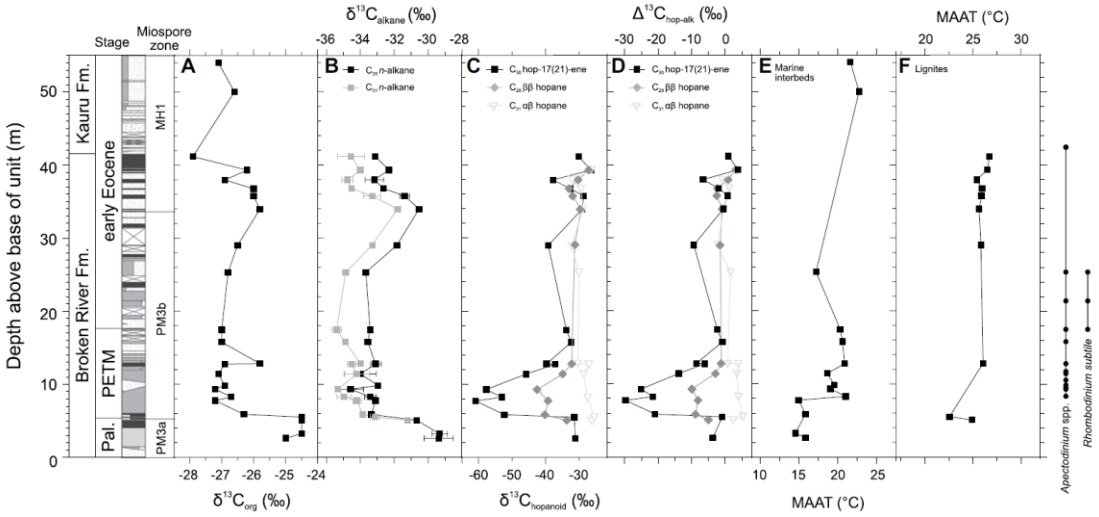

Figure 1. CH_4 cycle perturbations at the Otaio River, New Zealand, during the Paleocene-Eocene Thermal Maximum (PETM). Pal.—Paleocene. (A) Bulk organic matter $\delta_{13}C$ values. (B) C_{29} (black) and C_{31} (dark gray) *n*-alkane $\delta_{13}C$ values. (C) C_{30} hop-17(21)-ene (black square), C_{29} ββ hopane (dark gray diamond), and C_{31} αβ hopane (light gray triangle) $\delta_{13}C$ values. (D) C_{30} hop-17(21)-ene (black square), C_{29} ββ hopane (dark gray diamond), and C_{31} αβ hopane (light gray triangle) $\Delta_{13}C_{hop\text{-}alk}$ ($\delta_{13}C_{hopanoid} - \delta_{13}C_{alkane}$) values. (E) Mean annual air temperature (MAAT) estimates in marine interbeds. (F) MAAT estimates in lignite seams. Shaded region in E and F indicates 1σ error. Key biostratigraphic markers are also shown (black filled circles) (Pancost et al., 2013; Naafs et al., 2018).

3. 热化学岩石圈分异与克拉通地幔的起源

翻译人：冯婉仪 fengwy@sustech.edu.cn

Capitanio F A, Nebel O, Cawood P A. ***Thermochemical lithosphere differentiation and the origin of cratonic mantle*** *[J]. Nature, 2020, 588:89-94.*

https://doi.org/10.1038/s41586-020-2976-3

摘要：克拉通记录了大陆岩石圈形成的早期历史，但它们是如何成为地球上岩石圈最稳定的部分仍不得而知。在这里，我们提出了一种机制来解释大量熔体亏损的克拉通岩石圈地幔（CLM）是如何形成以及如何演化为稳定的克拉通。数值模型显示，在一个伸展的岩石圈之下，地球早期热的地幔物质发生大规模的减压熔融，熔体抽取之后在地球深处留下了大量亏损的地幔。脱水、固化的地幔阻止了进一步的变形，迫使应变迁移和冷却，从而将亏损的地幔同化到岩石圈中。应变局部化和固化之间的负反馈维持了长期的扩散延伸和大量亏损 CLM 的就位。在低压条件下 CLM 的形成及其深部的重新平衡重现了受深度-温度条件约束的太古代岩石圈的演化过程，而在太古宙克拉通中，高程度的亏损和熔体体积最好用岩石圈强度较低的模型来匹配。在这些对板块构造来说是可行的条件下，热化学分异有效地阻止了板块边缘的形成：裂谷作用和岩石圈俯冲作用是短暂的，并且作为残余结构嵌入到冷却的 CLM 中，重现了在太古代克拉通中发现的循环和再活化的环境。尽管它们在早期阶段经历了大约 5 亿年的大规模熔融和再循环过程，模拟的岩石圈逐渐演化和稳定，然后再循环和再活化作用变成周期性的。早期主要的熔融和再循环事件解释了原始冥古宙岩石圈和地壳的产生和消失，而后期稳定和周期性的再活化过程为太古代大陆克拉通的形成提供了背景。

ABSTRACT: Cratons record the early history of continental lithosphere formation, yet how they became the most enduring part of the lithosphere on Earth remains unknown. Here we propose a mechanism for the formation of large volumes of melt-depleted cratonic lithospheric mantle (CLM) and its evolution to stable cratons. Numerical models show large decompression melting of a hot, early Earth mantle beneath a stretching lithosphere, where melt extraction leaves large volumes of depleted mantle at depth. The dehydrated, stiffer mantle resists further deformation, forcing strain migration and cooling, thereby assimilating depleted mantle into the lithosphere. The negative

feedback between strain localization and stiffening sustains long-term diffused extension and emplacement of large amounts of depleted CLM. The formation of CLM at low pressure and its deeper re-equilibration reproduces the evolution of Archaean lithosphere constrained by depth–temperature conditions, whereas large degrees of depletion and melt volumes in Archaean cratons are best matched by models with lower lithospheric strength. Under these conditions, which are otherwise viable for plate tectonics, thermochemical differentiation effectively prevents yielding and formation of margins: rifting and lithosphere subduction are short lived and embedded in the cooling CLM as relict structures, reproducing the recycling and reworking environments that are found in Archaean cratons. Although they undergo major melting and extensive recycling during an early stage lasting approximately 500 million years, the modelled lithospheres progressively differentiate and stabilize, and then recycling and reworking become episodic. Early major melting and recycling events explain the production and loss of primordial Hadean lithosphere and crust, whereas later stabilization and episodic reworking provides a context for the creation of continental cratons in the Archaean era.

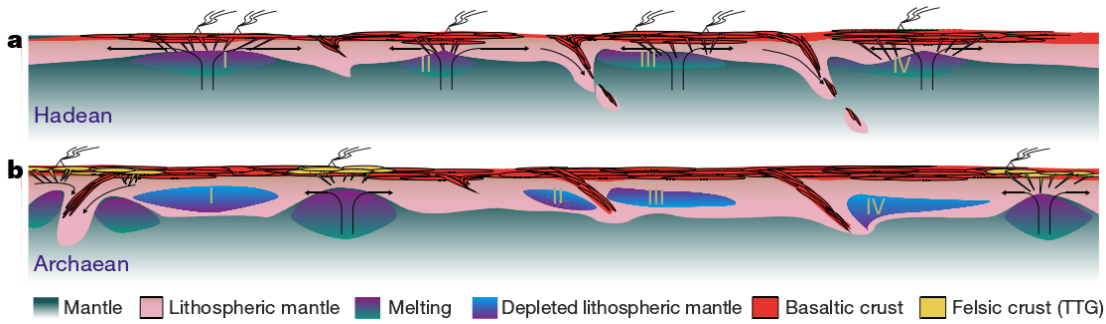

Figure 1. Sketch of the thermochemical differentiation of the lithosphere and the stabilization to form a craton. a, Initial proto-rifts and proto-convergent margins lead to the formation and recycling of primordial lithosphere (pink) and basaltic crust (red), above large volumes of mantle melting (green–purple, i to iv). This is a likely condition in the Hadean. b, The stiffening of the mantle as melt is extracted forces the migration of rifting and the embedding of large volumes of depleted mantle into the lithosphere (blue–purple, i to iv). The progressive stiffening favours thickening and stabilization in the Archean, and the demise of proto-margins. Minor rifting and subduction-like downwellings allow intra-crustal melting and the differentiation of primordial basaltic crust into a felsic, TTG-like crust (yellow).

4. 海底热液循环通道的磁成像

翻译人：李园洁 liyj3@sustech.edu.cn

*Galley G., Jamieson W., Lelièvre G., Farquharson G., Parianos M.. **Magnetic imaging of subseafloor hydrothermal fluid circulation pathways[J]**. Science Advances, 2020 ,6(44):eabc6844. https://doi.org/10.1126/sciadv.abc6844*

摘要：海底热液循环是固体地球和之上海洋之间的化学和热传递的一个重要过程。海底热液的喷出可为生物群落提供场所，还可产生有价值的矿床。我们对海底热液循环系统的尺寸和几何状态的认识仅限于数值模拟和他们在海底的形态。本文中作者利用磁反演模拟第一次建立热液对流系统的三维经验模型。与流体循环相关的高温流体-岩石相互作用破坏了洋壳中的磁性矿物，使得磁模型可以追踪到热液通道。文中将这个模拟方法应用到在东 Manus 洋盆的一个活跃热液区。

ABSTRACT：Hydrothermal fluid circulation beneath the seafloor is an important process for chemical and heat transfer between the solid Earth and overlying oceans. Discharge of hydrothermal fluids at the seafloor supports unique biological communities and can produce potentially valuable mineral deposits. Our understanding of the scale and geometry of subseafloor hydrothermal circulation has been limited to numerical simulations and their manifestations on the seafloor. Here, we use magnetic inverse modeling to generate the first three-dimensional empirical model of a hydrothermal convection system. High-temperature fluid-rock reactions associated with fluid circulation destroy magnetic minerals in the Earth's crust, thus allowing magnetic models to trace the fluid's pathways through the seafloor. We present an application of this modeling at a hydrothermally active region of the East Manus Basin.

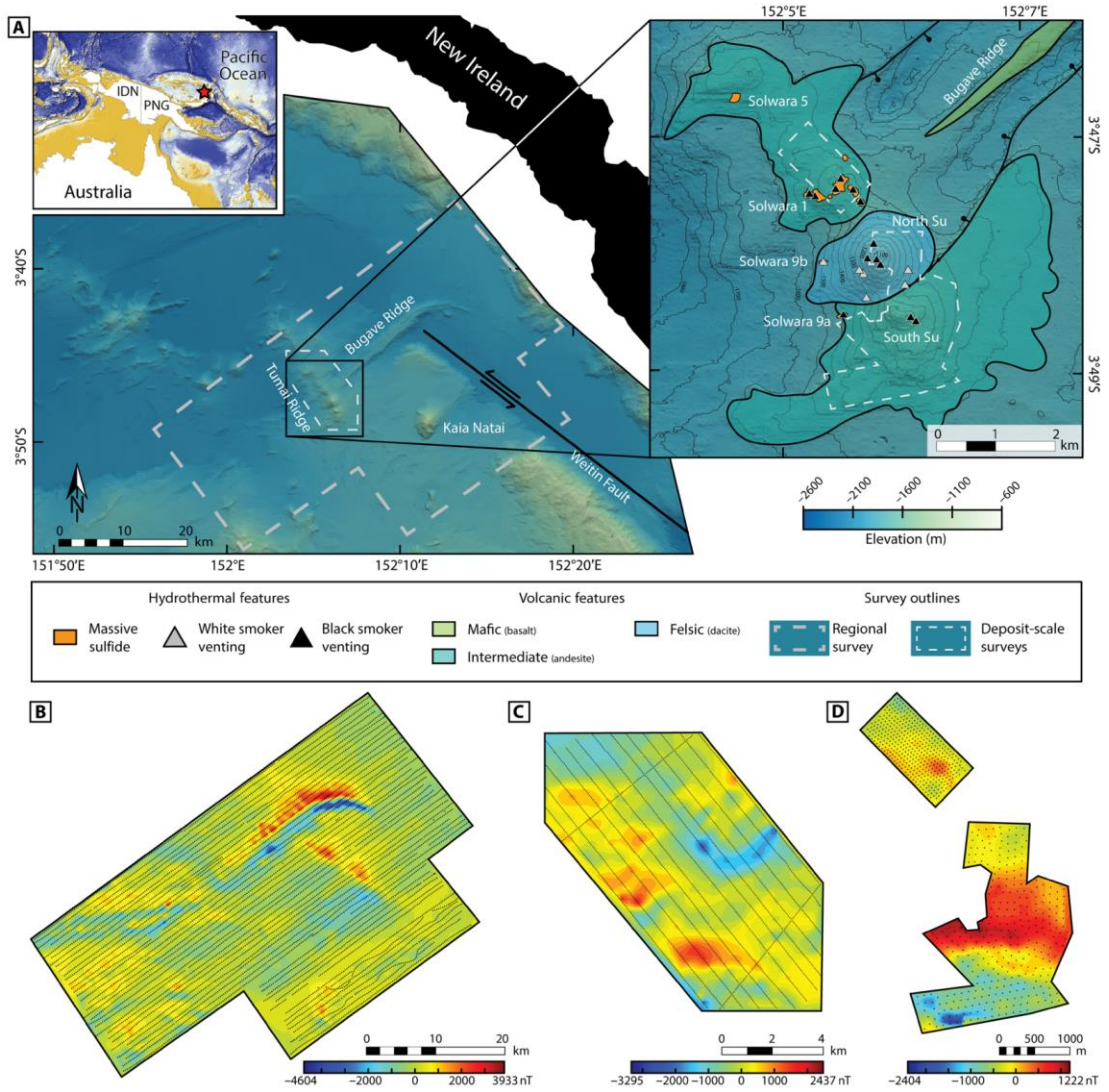

Figure 1. A map of the East Manus Basin in the region of the Tumai and Bugave Ridges, along with this study's total magnetic field anomaly maps. (A) A 35-m resolution bathymetric map of the East Manus Basin, centered about the Tumai Ridge and Bugave Ridge intersection. The inset map shows the major geological features near Susu Knolls and the locations of the known active and inactive hydrothermal vent sites along the Tumai Ridge, with 50-m bathymetric contour lines. Dashed gray and white lines represent the extents of the magnetic surveys. (B to D) Total magnetic field anomaly maps for the regional survey and both deposit-scale surveys, respectively. The black dots mark the positions of the measurement locations.

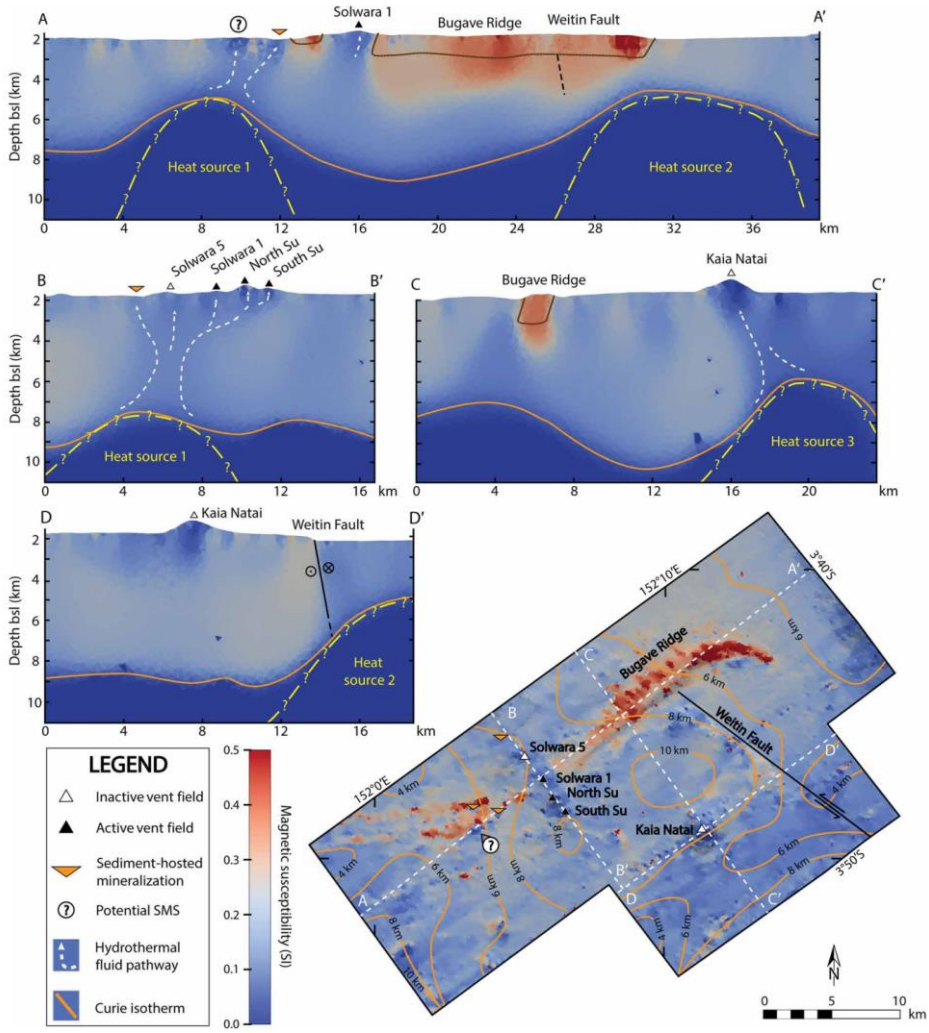

Figure 2. Map and cross sections of effective magnetic susceptibility from the regional 3D magnetic inversion model. A-A′ displays two prominent magnetic lows at ~2 km below the seafloor, which we interpreted to be magma chambers. The southwest magma chamber is the primary heat source driving hydrothermal circulation at Solwara 5 and Susu Knolls. B-B′ shows subseafloor high-temperature fluid pathways that feed the venting sites along the Tumai Ridge. C-C′ and D-D′ are two cross sections that pass through the hydrothermally active Kaia Natai volcano. The depth to the Curie isotherm is included on the plan view image as a contour map with orange lines, mapping the geometry of the underlying magmatic bodies.

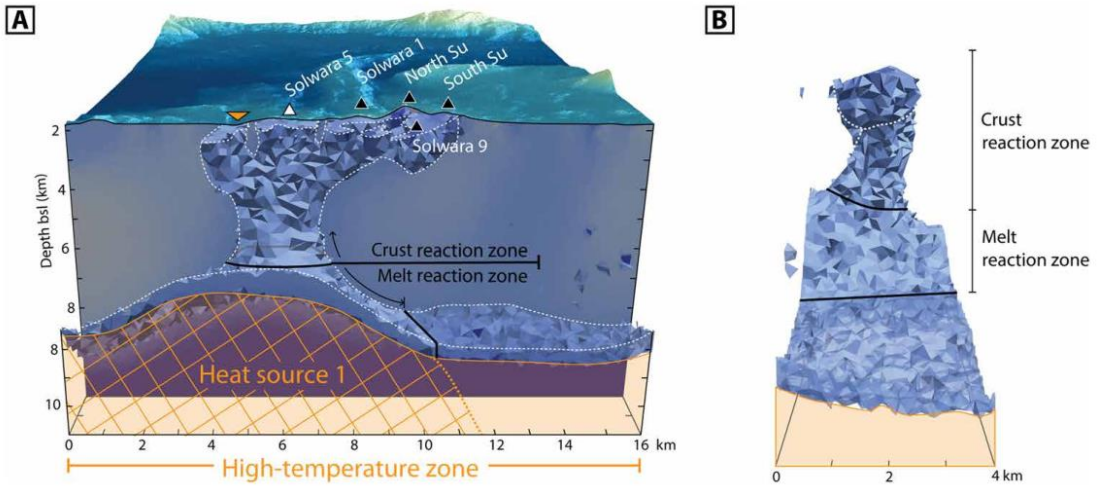

Figure 3. A 3D model of the high-temperature hydrothermal upflow column below the Tumai Ridge. The shown cross section is B-B′ from Fig. 2, with the alteration column visualized with a 0.12 SI threshold of the regional model’s effective magnetic susceptibility. (A) View of the column facing northeast. (B) View of the same column facing northwest. All surface hydrothermal feature symbols and the color scale follow the legend in Fig. 2.

5. 来自中欧的新的地磁长期变化数据二：古强度

翻译人：柳加波 Liujb@sustech.edu.cn

Schnepp E, Thallner D, Arneitz P, et al. ***New archeomagnetic secular variation data from Central Europe, II: Intensities****[J].* ***Physics of the Earth and Planetary Interiors****, 2020, 309: 106605.*

https://doi.org/10.1016/j.pepi.2020.106605

摘要：过去一千年中，地磁场的变化可以通过研究考古材料来获得。欧洲可用古数据的空间分布相当不均匀，只有大约 15%的站点提供了完整的地磁场矢量记录。在这里，我们报道了 39 个新的可靠的古强度数据，这些数据来自奥地利、德国和瑞士，年龄介于 1500 BCE 和 1900 CE 之间。对于其中的 31 个，方向信息也可用。古强度是用类 Thellier 方法，和多样本磁畴状态校正的古强度方法，或者同时使用这两种方法获得的。对考古建筑物样品进行了热剩磁各向异性的校正，在大多数情况下，仅显示了百分之几的微小变化。我们对 16 块考古建筑物样品进行了冷却速率依赖性测试，经常在实验过程中观察到强烈的变化。我们应用了七种成功的冷却速率校正，使古强度值降低了约 10%。从多样本技术获得的古强度值通常略低于 Thellier 实验获得的值。岩石磁学表明，磁铁矿型矿物主要在伪单畴范围内作为主要磁性载体，但也存在高矫顽性矿物成分，如赤铁矿或 ε 氧化铁。新数据与已公布的古强度基本吻合。它们支持在公元前 800 年左右和公元前 1000 年出现强烈的强度变化。新的全矢量古地磁数据显示，从公元前 850 年左右的德国数据中观察到低古强度伴随着偏角出现高达 50°的巨大变化。

ABSTRACT: Variations of the geomagnetic field during the past millennia can be obtained by investigating archeological material. The spatial distribution of the available data across Europe is rather uneven and only about 15% of the sites provide a full vector record of the geomagnetic field. Here we report 39 new reliable paleointensity data for sites from Austria, Germany and Switzerland, with ages ranging between 1500 BCE and 1900 CE. For 31 of them, directional information is available, too. Paleointensities were determined with Thellier type techniques, with the multiple-specimen domain-state corrected paleointensity protocol or with both techniques. Corrections for anisotropy of thermoremanent magnetization were carried out for the structures, showing small variations of only a few per cent in most cases. Cooling rate dependence was tested for 16 structures.

Often strong alteration during the experiments was observed. Seven successful cooling rate corrections were applied, which lowered the paleointensity values by about 10%. Values obtained from the multiple-specimen technique are generally somewhat lower than those from the Thellier experiments. Rock magnetic measurements revealed magnetite-type minerals mostly in pseudo single domain range as main magnetic carrier, but also high coercive mineral components like hematite or epsilon iron oxide are present. The new data are mostly in good agreement with published paleointensities. They support the presence of strong intensity variations around 800 CE and in the millennium BCE. The new full vector data reveal that the deep paleointensity minimum observed from German data around 850 BCE is accompanied by large variations in direction with declinations up to 50°.

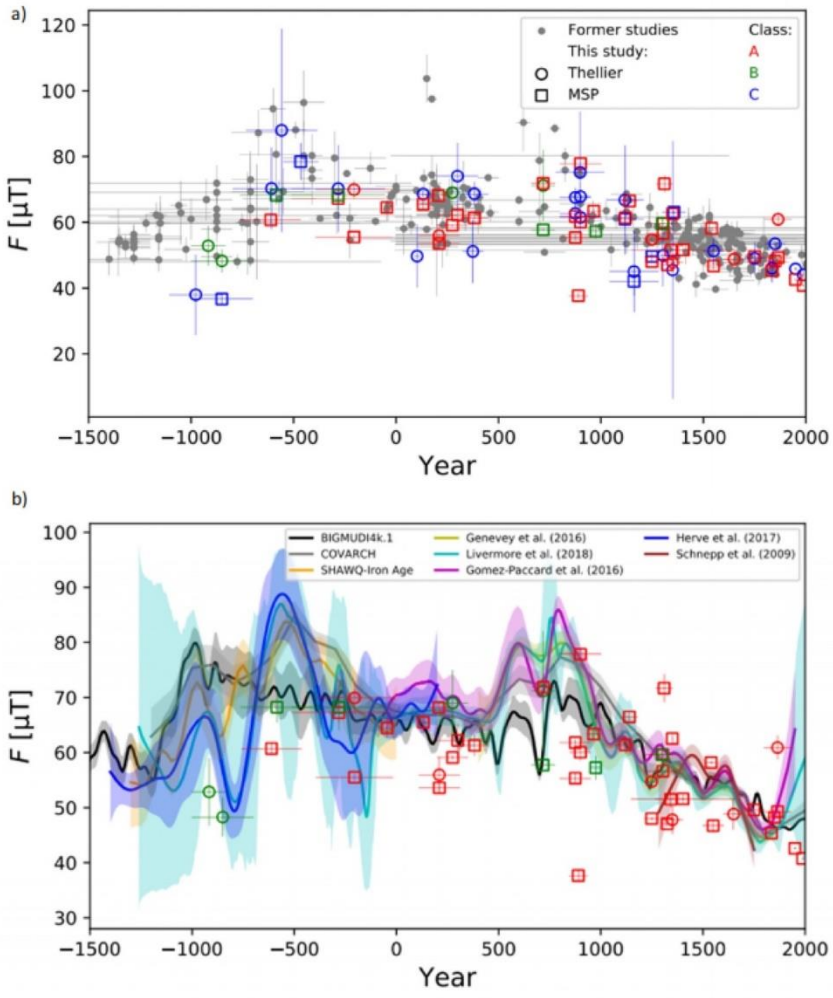

Figure 1. a) Comparison of new archeointensity data and other available records within a 750 km radius around Nuremberg (49.5°N, 11.1°E). b) New high quality data (i.e. Class A and B from a) compared to global and regional field model curves.

6. 拉萨地块（西藏）从冈瓦纳到欧亚大陆中生代漂移的古地磁约束

翻译人：周洋 zhouy3@sustech.edu.cn

Li Z Y, Ding L, Peter C L, et al. ***Paleomagnetic constraints on the Mesozoic drift of the Lhasa terrane (Tibet) from Gondwana to Eurasia*** *[J].* ***Geology****, 2016, 44（9）：727－730.*
http://pubs.geoscienceworld.org/gsa/geology/article-pdf/44/9/727/3550113/727

摘要：青藏高原来源于冈瓦纳的地块，其中生代构造演化一直存在广泛争议，到目前为止，关于其古纬度漂移的古地磁约束仍然很少。在论文中，我们汇总了主要在中文文献中发表的的数据，从拉萨地块 180Ma 的 Sangri 群火山岩中获得了一个新的、高质量的古地磁极，古纬度显示为 3.7°S±3.4°。新的极点表明拉萨地块在三叠纪晚期从冈瓦纳裂解、漂移，而不是人们普遍认为的二叠纪。在 220-130 Ma 期间，大约向北漂移了 4500 公里，板块南北向平均运动速率为 5 cm / yr。我们认为拉萨地块来源于印度或澳大利亚。

ABSTRACT: The Mesozoic plate tectonic history of Gondwana-derived crustal blocks of the Tibetan Plateau is hotly debated, but so far, paleomagnetic constraints quantifying their paleolatitude drift history remain sparse. Here, we compile existing data published mainly in Chinese literature and provide a new, high-quality, well-dated paleomagnetic pole from the ca. 180 Ma Sangri Group volcanic rocks of the Lhasa terrane that yields a paleolatitude of 3.7°S ± 3.4°. This new pole confrms a trend in the data that suggests that Lhasa drifted away from Gondwana in Late Triassic time, instead of Permian time as widely perceived. A total northward drift of ~4500 km between ca. 220 and ca. 130 Ma yields an average south-north plate motion rate of 5 cm/yr. Our results are consistent with either an Indian or an Australian provenance of Lhasa.

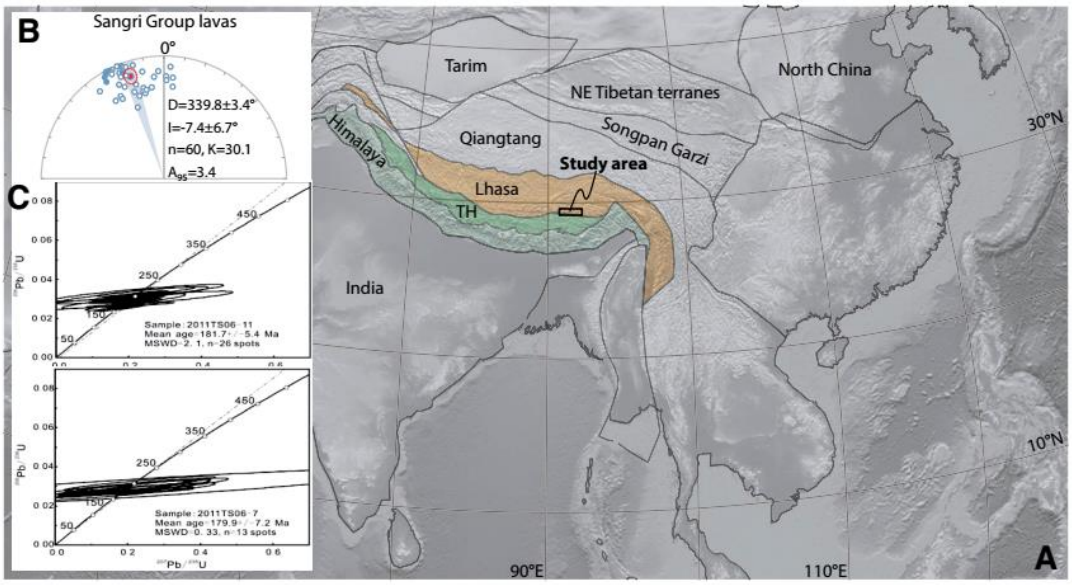

Figure 1. A: Schematic tectonic map of Tibet showing study area of Sangri Group lavas and outlines of Lhasa block and Tibetan Himalaya (TH). B: Lava site average paleomagnetic directions of Sangri Group lavas (D— declination; I—inclination; K—Fisher precision parameter). C: Zircon U-Pb ages of two samples of Sangri Group lavas (MSWD—mean square of weighted deviates).

7. 古菲律宾海板块的特征:来自菲律宾东部海域岩石圈碎片的证据

翻译人：刘伟 inewway@163.com

Carla, Dimalanta B , Decibel, et al. Characterization of the proto-Philippine Sea Plate:Evidence from the emplaced oceanic lithospheric fragments along eastern Philippines[J]. Geoscience Frontiers, 2020, v.11(01):8-26.

https://doi.org/10.1029/2020JB019758

摘要：菲律宾群岛中生代超俯冲蛇绿岩已被许多学者解释为古菲律宾海板块(pPSP)。本文对菲律宾东部的蛇绿岩进行了综述。本文介绍了吕宋岛(Isabela、Lagonoy in Camarines north 和 Rapu-Rapu island)、菲律宾中部(Samar、Tacloban、Malitbog 和 Bohol 东南部)和棉兰老岛（Mindanao）东部(Dinagat 和 Pujada)海洋岩石圈碎片的地质学、年代学和地球化学特征。菲律宾南部的 Halmahera 蛇绿岩的特征也用来作比较。沿菲律宾东部保存的几乎所有地壳-地幔序列都具有早白垩世至晚白垩世的年代特征。地幔和地壳剖面的地球化学特征反映了洋中脊和超俯冲的特征。虽然目前的古地磁信息仅局限于 Samar 蛇绿岩，但结果表明其为近赤道附近的中生代超俯冲带起源。通过对菲律宾东缘地壳-地幔序列的对比分析，认为它们可能是中生代古菲律宾海板块的碎片。

ABSTRACT: The proto-Philippine Sea Plate (pPSP) has been proposed by several authors to account for the origin of the Mesozoic supra-subduction ophiolites along the Philippine archipelago. In this paper, a comprehensive review of the ophiolites in the eastern portion of the Philippines is undertaken. Available data on the geology, ages and geochemical signatures of the oceanic lithospheric fragments in Luzon (Isabela, Lagonoy in Camarines Norte, and Rapu-Rapu island), Central Philippines (Samar, Tacloban, Malitbog and Southeast Bohol), and eastern Mindanao (Dinagat and Pujada) are presented. Characteristics of the Halmahera Ophiolite to the south of the Philippines are also reviewed for comparison. Nearly all of the crust-mantle sequences preserved along the eastern Philippines share Early to Late Cretaceous ages. The geochemical signatures of mantle and crustal sections reflect both mid-oceanic ridge and supra-subduction signatures. Although paleomagnetic information is currently limited to the Samar Ophiolite, results indicate a near-equatorial Mesozoic supra-subduction zone origin. In general, correlation of the crust-mantle

sequences along the eastern edge of the Philippines reveal that they likely are fragments of the Mesozoic pPSP..

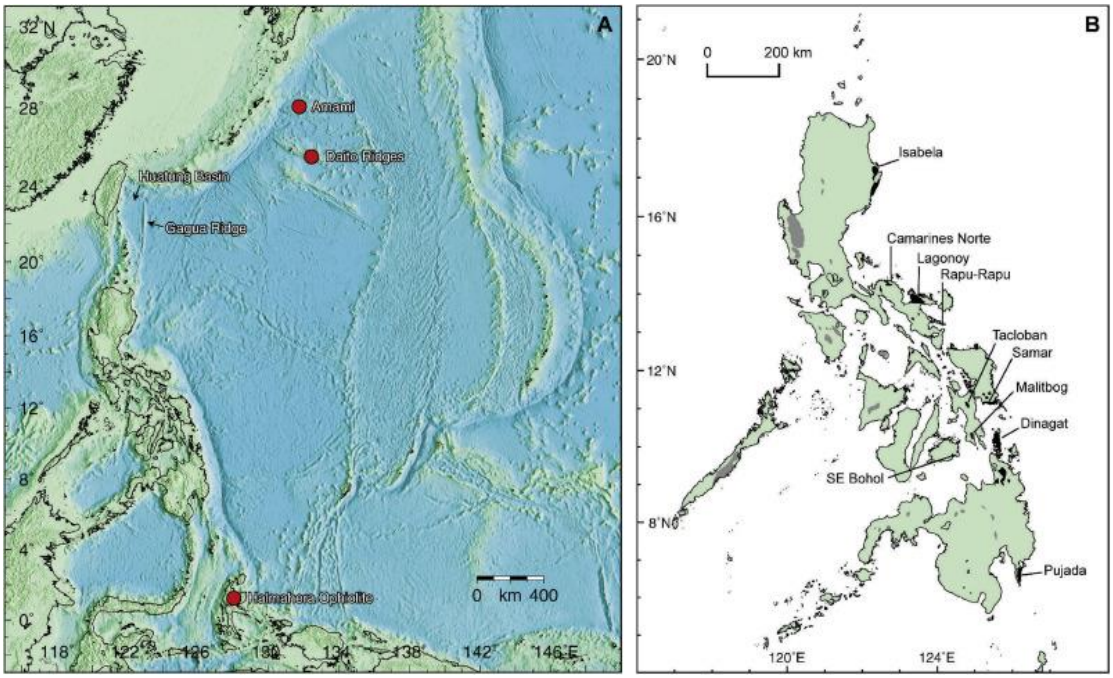

Figure 1. (A) Mesozoic terranes present east of the Philippine archipelago. (B) Map showing the ophiolites along the eastern portion of the Philippine archipelago. Gray areas show the occurrence of ophiolites in the western portion of the Philippines, while the black portions indicate the location of ophiolites along eastern Philippines as discussed in this study.

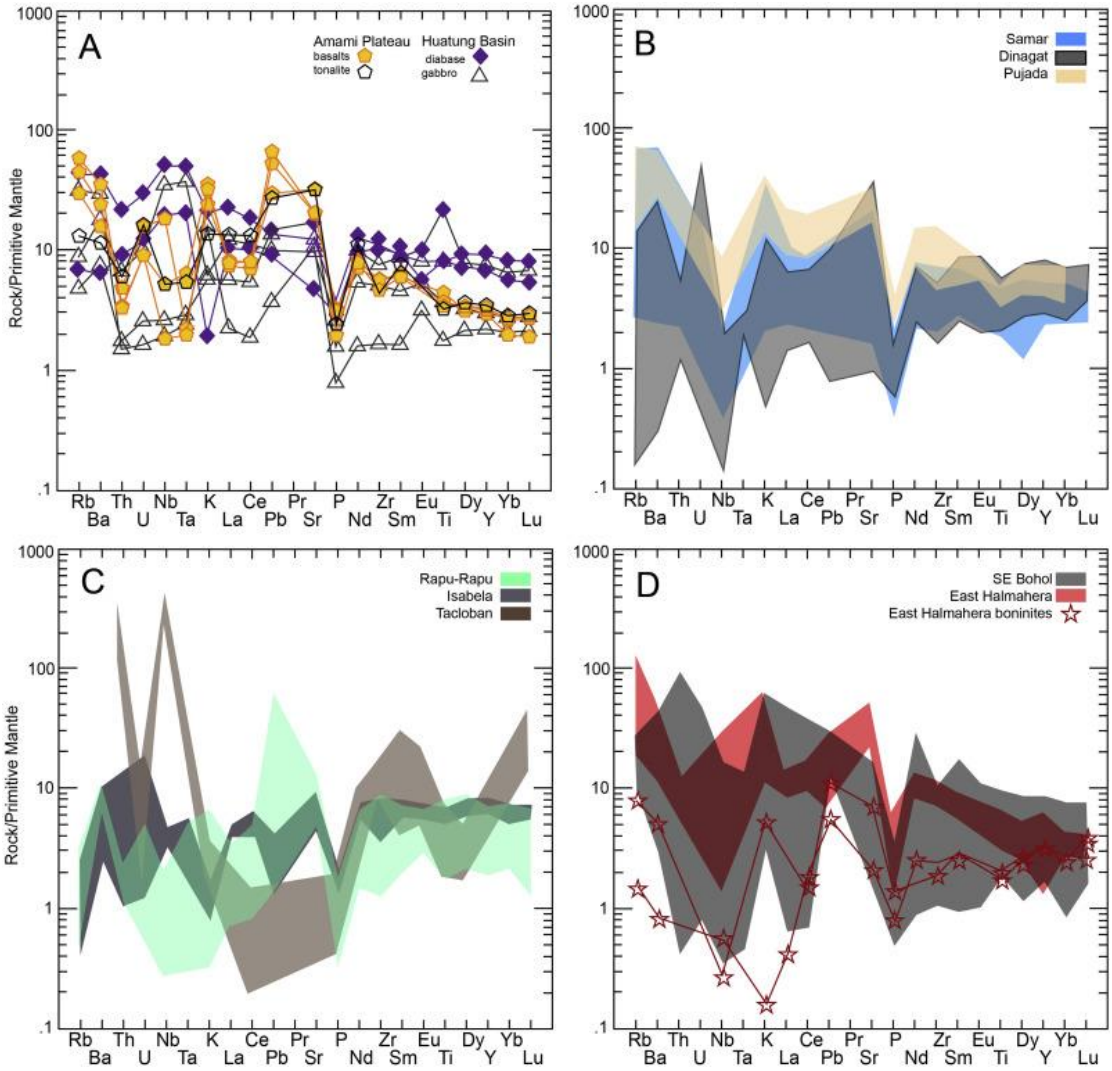

Figure 2. Plots showing primitive mantle normalized trace element of igneous rocks from (A) Huatung Basin and Amami Plateau (data from Hickey-Vargas, 2005 and Hickey-Vargas et al., 2008), (B) Samar, Dinagat and Pujada, (C) Rapu-Rapu, Isabela and Tacloban and (D) SE Bohol and East Halmahera. Normalizing values are from Sun and McDonough (1989).

8. 青藏高原季节性升温异常对东亚夏季风降水的先驱影响

翻译人：杨会会 11849590@mail.sustech.edu.cn

Duan A M, Hu D, Hu W T and et al. ***Precursor effect of the Tibetan Plateau Heating Anomaly on the Seasonal March of the East Asian Summer Monsoon Precipitation****[J].****Journal of Geophysical Research:Atmospheres****, 125, e2020JD032948.*

https://doi.org/10.1111/bor.12484. ISSN 0300-9483

摘要：东亚夏季风驱动因素复杂，主要表现为主雨带的突发性和向北移动。通过对 1961-2016 年多来源观测资料的再分析，本文讨论了青藏高原前期非绝热加热与东亚夏季风季节变化之间的关系。结果表明:青藏高原上空的地表感热异常和凝结热异常分别使华南雨季（东亚夏季风第一阶段）的开始、持续时间和总降水分别提前 2 个月和 1 个月左右。在西南地区雨季（东亚夏季风第二阶段）开始前 1 个月左右，高原上空有明显的正凝结加热异常。相比之下，在东亚夏季风剩余阶段，青藏高原的升温与雨季开始的关系相对较弱，包括梅雨和华北雨季。结果表明，青藏高原的强加热使低层西南环流向东南方向加强，促进了水汽的辐合和上升运动，导致雨季提前到来。线性斜压模式的敏感性实验进一步证实了青藏高原的加热产生的环流条件，有利于对华南和西南地区雨季的开始。青藏高原热力异常是东亚夏季风早期启动的先驱。

ABSTRACT: The East Asian summer monsoon (EASM) has complex drivers and is characterized by an abrupt onset and northward jumps of the main rain band. By analyzing multisource observational data and reanalysis data sets during 1961–2016, we addressed the connection between the preceding diabatic heating of the Tibetan Plateau (TP) and the seasonal march of the EASM. We show that the positive surface sensible heating and condensation heating anomalies over the TP lead the onset, duration, and total precipitation of the rainy season in South China (the first stage of the EASM) by about 2 and 1 month, respectively. A significant positive condensation heating anomaly over the TP can be detected about 1 month before the onset of the rainy season in Southwest China (the second stage of the EASM). By contrast, the relationship between heating of the TP and the

onset of the rainy season is relatively weak during the remaining stages of the EASM, including the Meiyu and North China rainy seasons. We suggest that the strong heating of the TP intensifies the low‐level southwesterly circulation to the southeast and facilitates the convergence of moisture and ascending motion, leading to an earlier onset of the rainy season. Sensitive experiments with a linear baroclinic model further confirmed the role of heating of the TP in generating circulation conditions favorable for the onset of the rainy season in both South and Southwest China. The TP heating anomaly therefore acts as a precursor of the early stage onset of the EASM.

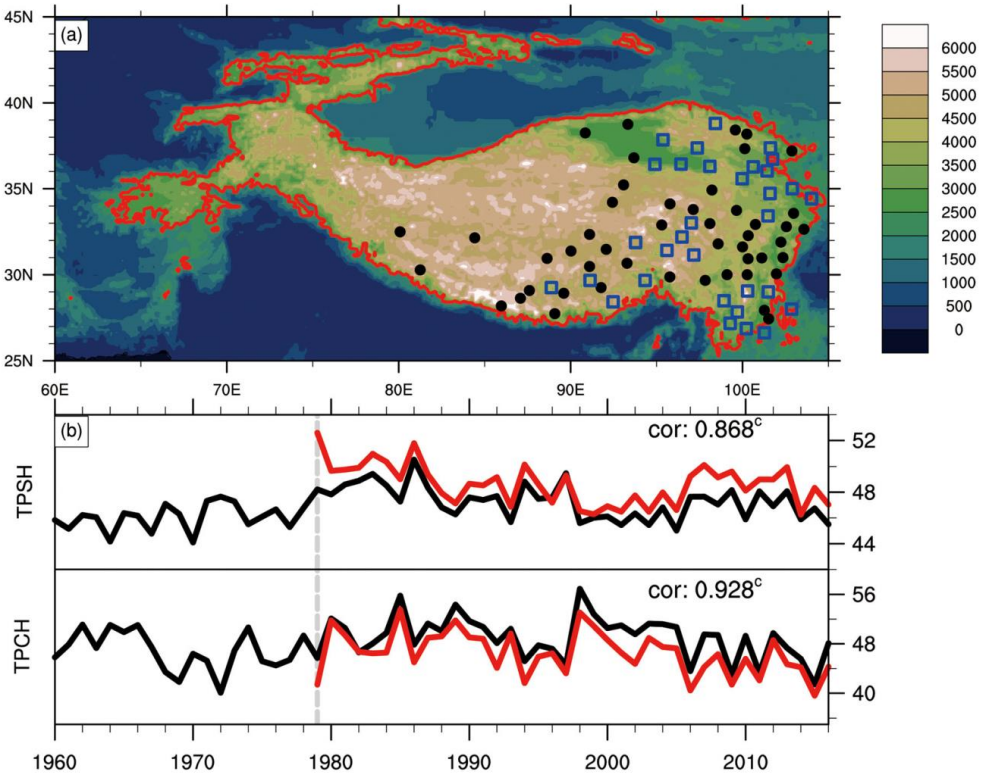

Figure 1. (a) Distribution of the 80 routine meteorology stations over the Tibetan Plateau. The squares and solid circles represent the 32 stations covering 1960–2016 and the 48 stations covering 1979–2016, respectively. The colors denote the altitude (units: m). The red curve shows the area of the Tibetan Plateau with an average altitude >2,500 m. (b) Temporal evolution of the annual mean 32 (80) ‐ station average Tibetan Plateau sensible heat flux (TPSH) and heat of condensation (TPCH) (units: W m−2). The black and red curves represent the 32 ‐ station and 80 ‐ station averages, respectively, and the correlation coefficients between them during the time period 1979 ‐ 2016 are marked in the top right of each panel. Statistical significance is shown by superscript letters: (a) $p < 0.1$, (b) $p < 0.05$, and (c) $p < 0.01$, hereafter.

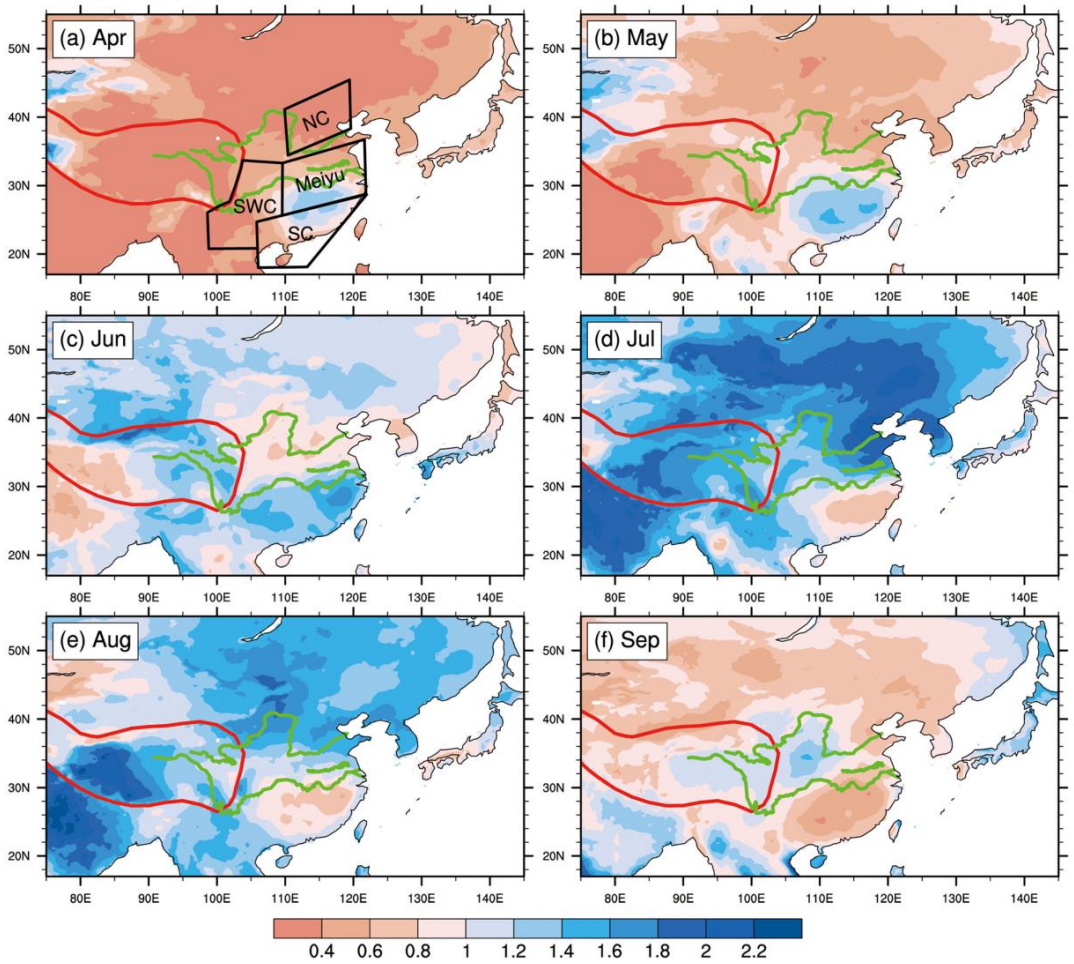

Figure 2. Ratio of the monthly precipitation in (a) April, (b) May, (c) June, (d) July, (e) August, and (f) September to the average precipitation from April to September during the time period 1960–2015. The three green curves from south to north denote the Yangtze, Huaihe, and Yellow Rivers, respectively, and the red curve denotes region of the Tibetan Plateau with an altitude >2,500 m. The black frames in part (a) denote the rough outline of the South China (SC), Southwest China (SWC), Meiyu, and North China (NC) regions.

9. 探索考古地球物理学中收集的数据一致性：来自 Villasviejas del Tamuja（西班牙埃斯特马杜）铁器时代希尔夫特的案例研究

翻译人：曹伟 11930854@QQ.com

Pro C, Caldeira B, Tena M T D , Charro C, Mayoral V. ***Exploring the Consistency of Data Collected in Archaeological Geophysics: A Case Study from the Iron Age Hillfort of Villasviejas del Tamuja (Extremadura, Spain)****.[J].* ***Remote Sensing****, 2020, 12:1989.*

https://doi.org/10.3390/rs12121989

摘要：在 Villasviejas del Tamuja（西班牙 Botija）定居点应用的不同地球物理方法已识别出位于同一位置的明显异常，但一些异常仅通过各自方法所反映。然而分析这些异常的空间相关性对于获得正确的考古解释具有重要意义。在本项研究中，我们分析了电阻率层析成像（ERT）、探地雷达（GPR）和磁梯度测量方法在考古遗址特定区域的测量结果。在数据分析中，我们对异常进行了图形和数值空间相关分析，发现各种方法提供的结果之间有很强的一致性，同时一些异常仅在磁测和 ERT 研究中获得响应。这些研究结果反映了多种地球物理方法联合应用和数据空间相关性分析的重要性。此外，我们应用于评估空间相关性的方法提供了有趣的结果。

ABSTRACT: Different geophysical methods applied at the settlement of Villasviejas del Tamuja (Botija, Spain) have identified robust anomalies located at the same position, but some anomalies are reflected by only one method. Furthermore, analysing the spatial correlation of these anomalies is of fundamental importance for obtaining a correct archaeological interpretation. In this work, we analysed the main results of electrical resistivity tomography (ERT), ground-penetrating radar (GPR) and magnetic gradiometry methods in a particular area of the archaeological site. In this analysis, we performed graphical and numerical spatial correlation analyses of the anomalies and observed strong agreement among the results provided by each method. Certain anomalies were reflected only in the magnetic and ERT studies. The results highlight the importance of applying several geophysical methods and performing spatial correlational analyses. Furthermore, the methodology that we have applied to evaluate the spatial correlation offers interesting results.

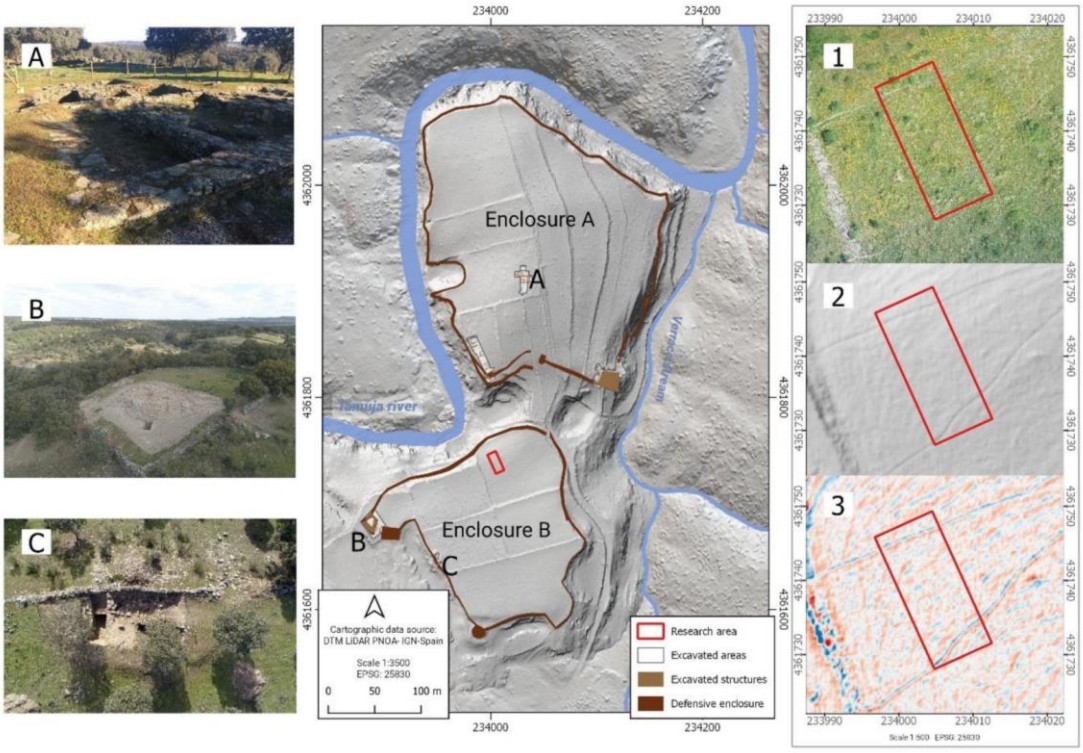

Figure 1. LiDAR digital terrain model (DTM) image of the study area. Photographs (A–C) show excavated areas, and the red rectangle in enclosure B corresponds to the zone analysed in this work. Images on the right show the research area in an orthophotograph (1), LiDAR DTM hillshade (2) and simple local relief model (SLRM) derived from the LiDAR DTM (3).

10. 不同细菌和培养温度对微生物合成磁铁矿与锰替代磁铁矿纳米颗粒的影响

翻译人：王敦繁 dunfan-W@foxmail.com

Roh Y, Jang H D, Suh Y. ***Microbial Synthesis of Magnetite and Mn-Substituted Magnetite Nanoparticles: Influence of Bacteria and Incubation Temperature****[J].* ***Journal of Nanoence and Nanotechnology****, 2007.*

https://doi.org/10.1166/jnn.2007.076

摘要：微生物合成磁铁矿和金属(Co, Cr, Ni)替代磁铁矿的研究最近才有报道。本研究的目的是考察 Mn 离子对微生物合成磁铁矿纳米颗粒的影响。研究了希瓦氏菌(PV-4)和热厌氧菌在中性 pH (pH = 7-8)的厌氧条件下对水铁矿或锰取代水铁矿的还原生物转化。这两种细菌都使用赤绿石作为磁铁矿前体形成了磁铁矿纳米颗粒。相比之下的磁铁矿由 PV-4 并使用 Mn 替代四方纤铁矿为前体,这是表明 PV-4 可以形成菱铁矿和磁铁矿在 25 C,而 TOR-39 形成主要的微米级别的磁铁矿在 60 C。通过能量色散 x 射线分析(EDX)发现，TOR-39 形成的磁铁矿中存在锰，表明锰被磁铁矿晶体取代。对 PV-4 形成的铁矿物的 EDX 分析表明，Mn 优先富集于菱铁矿和绿铁锈中。这些结果说明共沉淀或 Mn 诱导微生物形成菱铁矿和绿锈, 但 TOR-39 在 60 C 下形成 Mn 替代磁铁矿纳米颗粒。这些结果表明，该细菌具有合成磁铁矿和锰取代磁铁矿纳米晶体的能力。在近环境温度下，微生物促进磁铁矿和金属取代磁铁矿的合成可能扩大特殊铁磁纳米粒子的用途。

ABSTRACT: Microbial synthesis of magnetite and metal (Co, Cr, Ni)-substituted magnetites has only recently been reported. The objective of this study was to examine the influence of Mn ion on the microbial synthesis of magnetite nanoparticles. The reductive biotransformation of an akaganeite or a Mn-substituted akaganeite by Shewanella loiha (PV-4) and Thermoanaerobacter ethanolicus (TOR-39) was investigated under anaerobic conditions at circumneutral pH (pH = 7–8). Both bacteria formed magnetite nanoparticles using akaganeite as a magnetite precursor. By comparison of iron minerals formed by PV-4 and TOR-39 using Mn-mixed akaganeite as the precursor, it was shown that PV-4 formed siderite, and magnetite at 25 C, whereas TOR-39 formed mainly nm-sized magnetite at 60 C. The presence of Mn in the magnetite formed by TOR-39 was

revealed by energy dispersive X-ray analysis (EDX) is indicative of Mn substitution into magnetite crystals. EDX analysis of iron minerals formed by PV-4 showed that Mn was preferentially concentrated in the siderite and green rust. These results demonstrate that coprecipitated/sorbed Mn induced microbial formation of siderite and green rust by PV-4 at 25 C, but the synthesis of Mn-substituted magnetite nanoparticles proceeded by TOR-39 at 60 C. These results indicate that the bacteria have the ability to synthesize magnetite and Mn-substituted magnetite nano-crystals. Microbially facilitated synthesis of magnetite and metal-substituted magnetites at near ambient temperatures may expand the possible use of specialized ferromagnetic nano-particles.

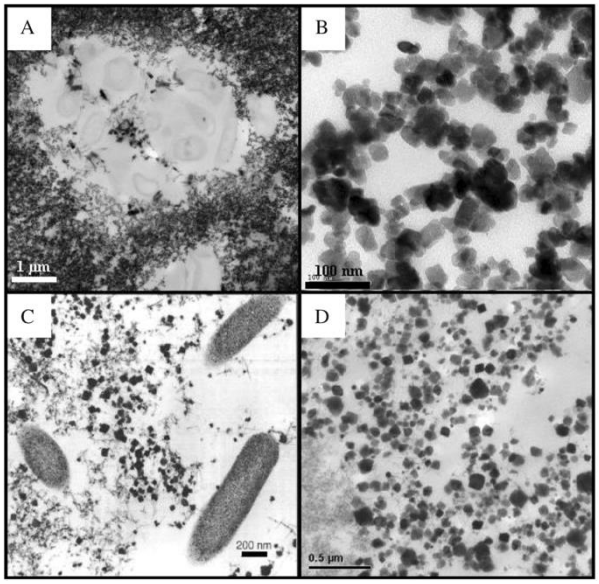

Figure 1. TEM images of magnetite nanoparticles formed by Shewanella loiha (PV-4) (A) at 25 C and magnetite nanoparticles formed by Thermoanaerobacter sp. (TOR-39) 60 C (C). TEM images of magnetite nanoparticles formed by PV-4 at 25 C (B) and TOR-39 at 60 C (D)

11. 古气候研究在中国考古中的尺度不匹配

翻译人：郑威　11930589@mail.sustech.edu.cn

Jaffe Y, Castellano L, Shelach-Lavi G, et al. ***Mismatches of scale in the application of paleoclimatic research to Chinese archaeology****[J].* ***Quaternary Research****, 2020: 1-20.*

https://doi.org/10.1017/qua.2020.60

摘要：围绕着关于考古和古气候轨迹关联性的艰巨任务直接影响了中国古代人地关系的研究。由于近期中国考古文献普遍认为4.2千年事件导致了中国多个区域新石器文明的崩溃，所以我们选择4.2千年事件作为研究重点。很多文献综述关心围绕着重建东亚地区4.2千年事件的许多问题，我们提供了三个来自长江下游，陕西黄土高原和中央平原的案例，详细说明了一系列关于在中国考古中使用气候变化作为社会政治变化的因果机制的问题。于是我们关注到一个很常见但是存在颇多问题的方法论——越来越多地使用《中国文物地图集》中的考古汇编数据来与气候指标做关联，以生成线性的因果模型来解释社会经济崩溃。我们以中国东北的一个例子为例，过去30多年的工作提供了丰富的数据，可以以更有效的方式来回答这些问题，并且为考古学家和气候学家未来的研究提出一些列的建议。

ABSTRACT: Issues surrounding the difficult task of correlating archaeological and climatic trajectories are directly impacting the study of human-environmental interaction in Ancient China. We have chosen to focus on the 4.2 ka BP event due to the widespread belief in recent Chinese archaeological publications that it brought about the collapse of Neolithic cultures in multiple regions of China. Following a literature review concerning the many issues surrounding the reconstruction of the 4.2 ka BP event in East Asia, we present three short case studies from the Lower Yangzi, the Shaanxi loess plateau, and the Central Plains detailing a number of problems with Chinese archaeological attempts at using climate change as a causal mechanism for sociopolitical change. We then focus on a common but highly problematic methodology—the growing use of archaeological data compiled in the Atlas of Chinese Cultural Relics to correlate with climate proxies in order to generate linear, causal models explaining sociopolitical collapse. We follow with an example from Northeast China, where work from the past three decades has provided ample data with which to begin answering these questions in a more productive manner,

and end with a set of suggestions for archaeologists and climate scientists going forward.

Figure 1. Common misconceptions of archaeological data.

12. 亚速尔群岛全矢量古长期变化曲线:为过去 2kyr 提供可靠的古地磁测年

翻译人：李海 12031330@mail.sustech.edu.cn

Li M, Zhu S, Ouyang T, et al. ***Magnetic properties of the surface sediments in the Yellow River Estuary and Laizhou Bay, Bohai Sea, China: Implications for monitoring heavy metals*** *[J]. Journal of Hazardous Materials, 2020, online.*

https://doi.org/10.1029/2020JB019745

摘要: 古地磁测年需要高精度的方向和古强度变化曲线。大西洋中部的亚速尔群岛提供了大量全新世以来的火山产物，使其成为一个从确定年代的熔岩流中收集古地磁数据与构建PSV曲线进行定年的理想场所。本次研究，我们提供了新的皮克岛全矢量古地磁数据，并与邻近岛屿的数据相结合，为亚速尔群岛构建了新的全矢量PSV曲线。广泛的岩石磁性研究为古地磁载体的质量提供基础。在皮克岛，我们获得了21个新的古地磁场方向，利用多种方法对12个点进行古强度估计，获得15个古强度值，并已知14和10号点位的年代。通过放射性碳年龄校准的非高斯不确定性以及与方向和古强度估计相关的置信区间，我们获得了亚速尔群岛第一个全矢量PSV曲线，其置信区间为2kyr。PSV曲线显示900-1560AD间为低倾角期，最小值为32°。我们成功的对皮克岛五处熔岩流进行了测定，证明我们新的全矢量PSV曲线的潜力。

ABSTRACT: For archaeomagnetic dating high quality directional and intensity paleosecular variation curves are needed. The Azores Archipelago in the Mid‐Atlantic Ocean provides a wealth of volcanic products erupted during the Holocene, making it an ideal location to (1) gather paleomagnetic data from well dated lava flows, and (2) construct a paleosecular variation (PSV) curve that enables paleomagnetic dating of volcanic products with unknown age. Here we present new full vector paleomagnetic data from Pico Island, and combine the new data with existing data from neighboring islands to construct a new full‐vector PSV curve for the Azores Archipelago. An extensive rock magnetic study underpins the quality of our paleomagnetic carriers. From Pico Island, we obtained 21 new mean site directions; and 15 paleointensity estimates with the multimethod paleointensity approach from 12 sites, the age was known for 14 and 10 sites, respectively. By bootstrapping the non‐Gaussian uncertainty estimates of the radiocarbon age calibrations and the confidence intervals associated with the direction and paleointensity estimates we produce the first

full - vector PSV curve with confidence intervals for the Azores covering the past 2 kyr. The PSV curve reveals a period of low inclination between ~900 – 1560 AD, with minimum values of 32°. The potential of our new full - vector PSV curve is demonstrated by successfully dating five lava flows from Pico Island.

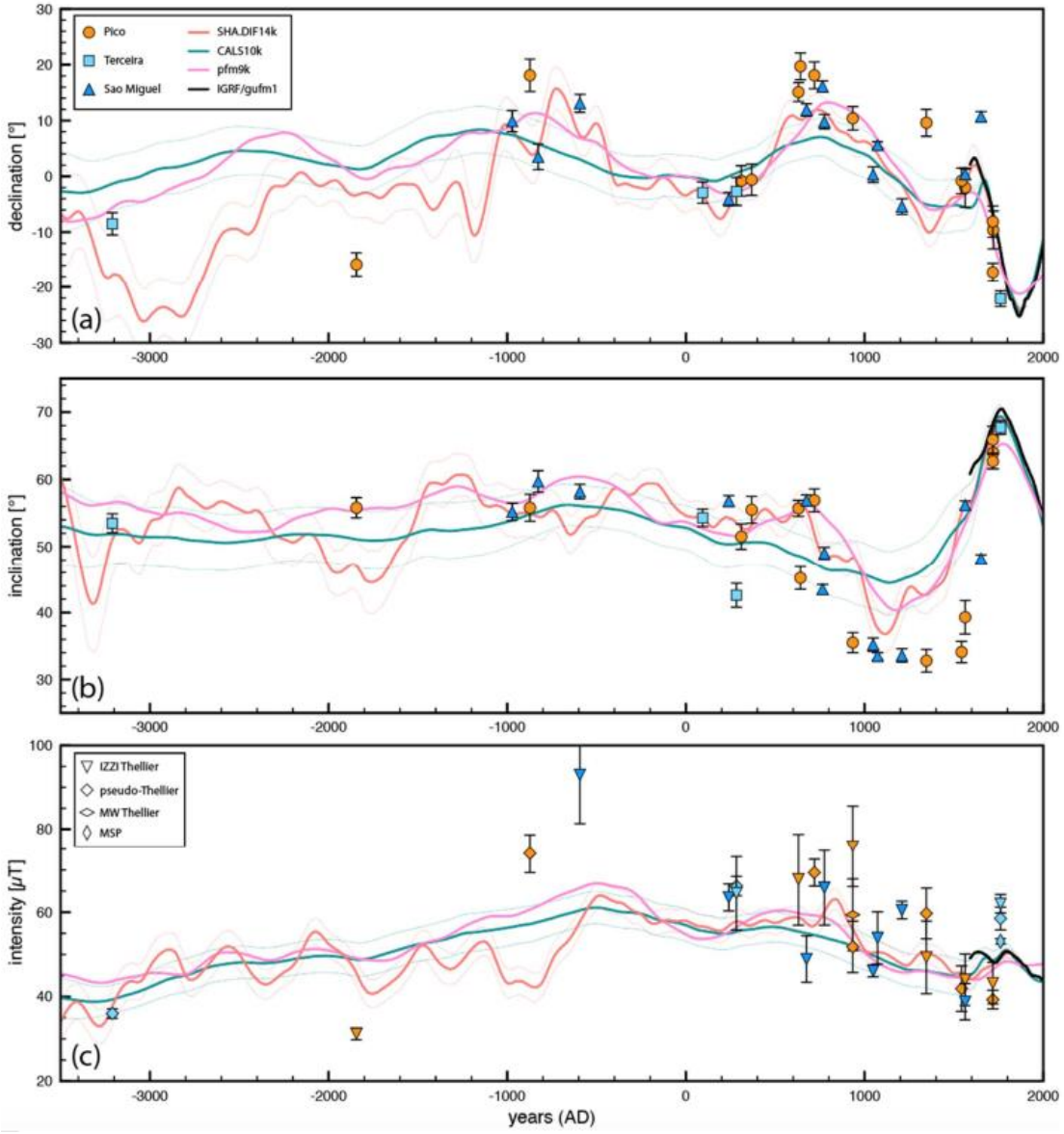

Figure 1. Full-vector geomagnetic field record for the Azores. The declination (a), inclination (b) and intensity (c) results are shown for Pico (orange, this study), Terceira (light blue, de Groot et al., 2016) and São Miguel (dark blue,Di Chiara et al., 2012; 2014b). Geomagnetic field models for Pico Island are presented by the colored lines: SHA.DIF.14k red lines (Pavón-Carrasco et al., 2014) including one standard deviation envelops; pfm9k pink line (Nilsson et al., 2014); CALS10k (Korte et al., 2011) including one standard deviation error envelops teal colored line; and the IGRF/gufm1 in black (Jackson

et al., 2000; Thébault et al., 2015). The declination and inclination data from Pico are depicted as orange circles with the associated error bars calculated from the α95 values (following calculations in Suttie & Nilsson, 2019). In the declination (a) and inclination (b) panels, data of Terceira are squares and from São Miguel are triangles; in the paleointensity panel (c), the shape of the data point reflects the paleointensity method used (see inset). The vertical error bars are the associated one standard deviation confidence intervals. The associated age errors are presented in Table 1 and supporting information S5.

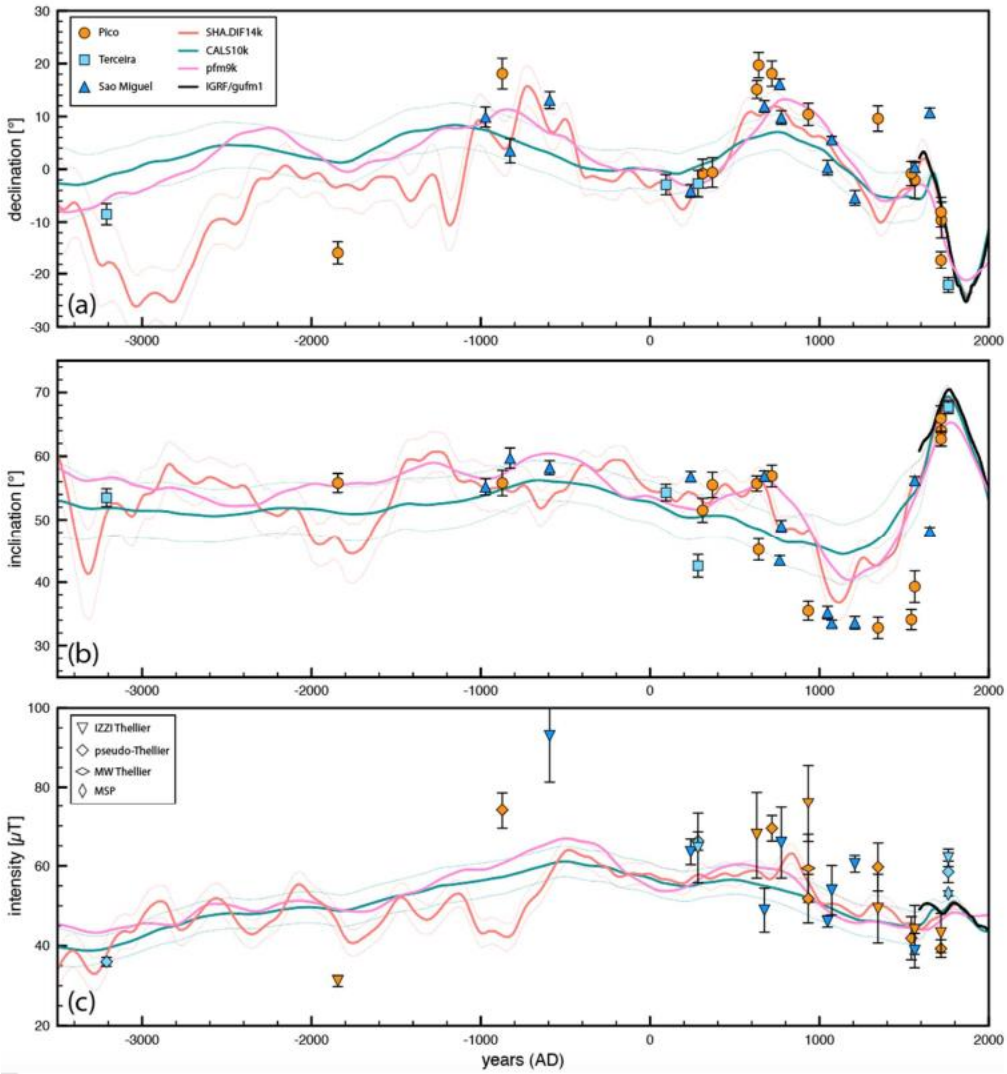

Figure 2. Full-vector paleosecular variation curves past 2 kyr for the Azores. The bootstrapped declination (a), inclination (b) and intensity (c) curves are shown with the 68 % and 95 % confidence error envelops. The data used to produce the curves are plotted in the appropriate graphs, symbols and colors used are the same as for Figure 4; the thin colored lines present the geomagnetic field models for Pico Island. The non-Gaussian age error distributions are considered in the bootstrap.

13. Bølling–Allerød 时期北美中纬度地区广泛的湿地发育

翻译人：张亚南 zhangyn3@mail.sustech.edu.cn

Eunji Byun, Hiromitsu Sato, Sharon A. ***Cowling et al. Extensive wetland development in mid-latitude North America during the Bølling–Allerød*** *[J].****Nature Geoscience****, 2021,14,30-35*

https://doi.org/10.1038/s41561-020-00669-x

摘要：美国中西部在末次冰消期的古生态重建表明，稀树草原的生物群落的扩张缺乏现代的相似过程。尽管它们的空间范围和持续时间长达几千年，但“非相似”生物群落的自然结构和环境驱动因素仍然时推测性的。我们利用回归分析，将森林群落组成和湿地范围联系起来，来确定特定的树木种类和森林单元来指示森林的广泛分布。我们重新编译了区域花粉的时间序列，来表明耐洪水类树木的短暂增加和在 Bølling–Allerød 时期（~14.6-12.8 ka）达到主导优势。总的来说，花粉记录、森林组成和湿地广泛分布的分析结果表明美国中西部存在着广泛的冰消期湿地（40-60%）这种广泛但短暂的湿地分布与 Bølling–Allerød 时期劳伦冰盖南部冰川融水的产生相一致。湿地的扩张和其在中纬度的位置对冰消期甲烷来源的动态变化具有一定影响；我们对甲烷的估计（~11Tg yr-1）与冰芯记录模型中甲烷北部来源的增强大致相当。新仙女木时期（~12.8-11.7 ka）劳伦冰盖局部性融水的减少，部分解释了为什么这种不相似的多湿地草原急剧减少，削弱了潜在的甲烷来源。

ABSTRACT: Palaeoecological reconstructions of the American Midwest during the last deglaciation suggest the expansion of parkland biomes lacking modern analogues. Despite their spatial extent and persistence over several millennia, the landscape configuration and environmental drivers for the ‘no analogue’ biomes remain speculative. Here we use regression analysis linking settlement-era forest composition and wetland extent to identify specific trees and forest units strongly indicative of high wetland prevalence. We then recompile a regional pollen time series to show transient increases in these flood-tolerant trees, with prominent peaks during the Bølling–Allerød interstadial (~14.6–12.8 thousand years ago). Taken together, the pollen records, and analyses of settlement-era forest composition and wetland prevalence, suggest the establishment of extensive deglacial wetlands in the American Midwest (40–60% of land cover). This extensive, yet

transient, wetland was possibly supported by southward discharge of Laurentide Ice Sheet meltwater during the Bølling–Allerød. The timing of this wetland expansion and its mid-latitude location have implications for deglacial methane source dynamics; our estimate of ~11 Tg yr−1 of methane is comparable to the northern source enhancement modelled from ice-core records. Regional decline of the Laurentide Ice Sheet meltwater discharge at the onset of the Younger Dryas (~12.8–11.7 thousand years ago) explains in part why these no-analogue wetland-rich parklands sharply declined, weakening this potential methane source.

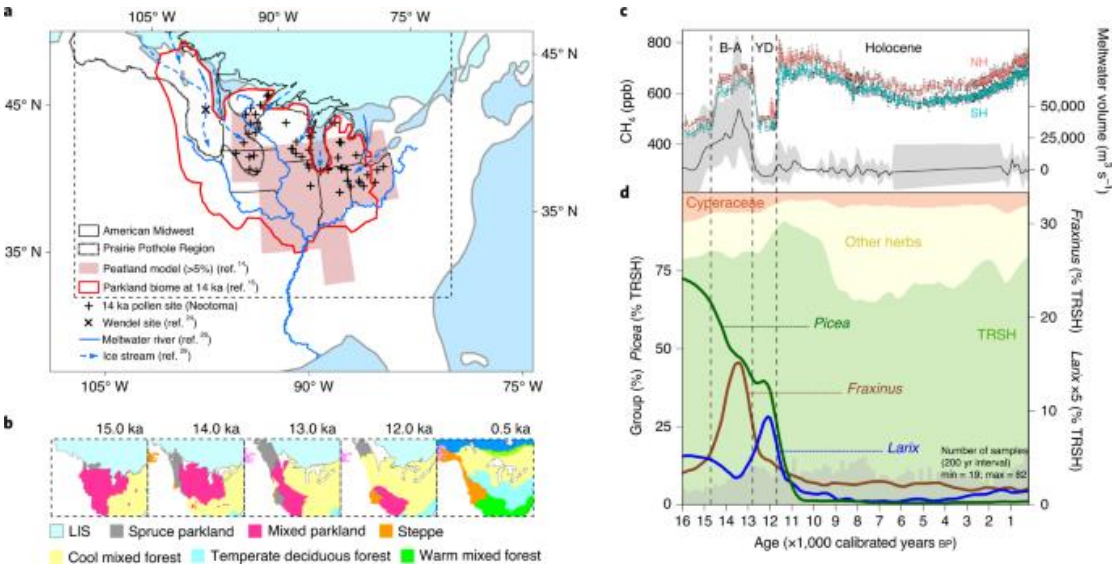

Figure 1. No-analogue biomes in palaeoenvironmental context. a, Spatial overlap of late-glacial parkland biomes, simulated peatland cover and LIS discharge. Dashed line indicates map's extent in b. b, Original graphics of pollen-derived biome maps. c, Atmospheric CH4 variations (1 s.d. errors) (NH, Northern Hemisphere; SH, Southern Hemisphere) and LIS discharge (black curve) (through the rivers highlighted in a; grey shading indicates the range of meltwater discharge from 2 s.d. errors of oxygen isotope records). d, Compiled pollen data (site locations in a) with the background stack showing relative abundance of grouped taxa and the smoothed curves for Picea, Fraxinus and Larix.

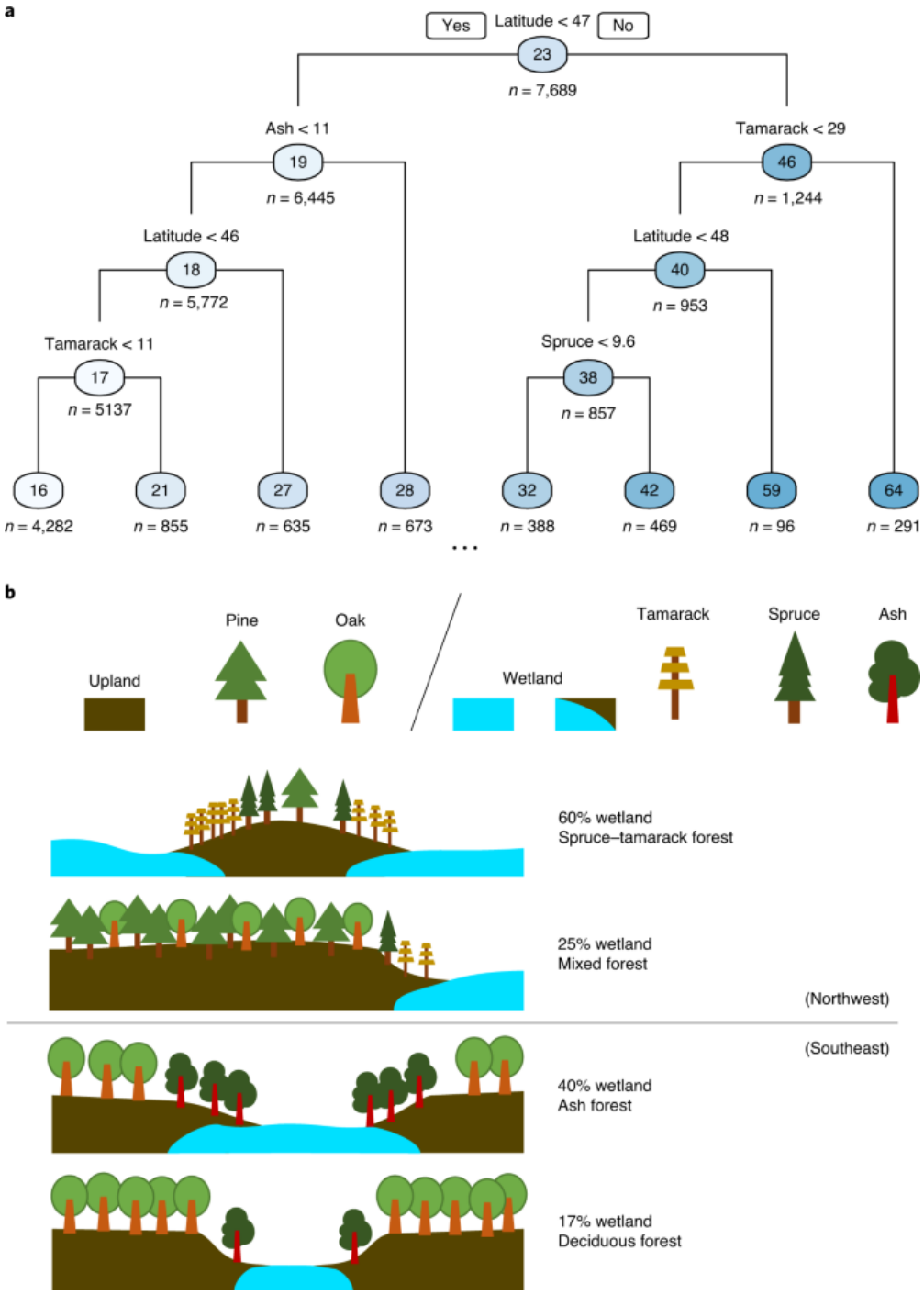

Figure 2. Regression analysis to predict percentage wetland area from forest composition. a, Sample regression tree model showing the three most important settlement-era trees and mean of wetland percentages in each node (shaded circles). b, Schematic showing typical forest compositions resulting from different levels of landscape wetness. Spruce–tamarack forest is the primary type towards the northwest and ash forest towards the southeast of the American Midwest (% wetland surface from Supplementary Tables 5 and 6). Symbols are not scaled.

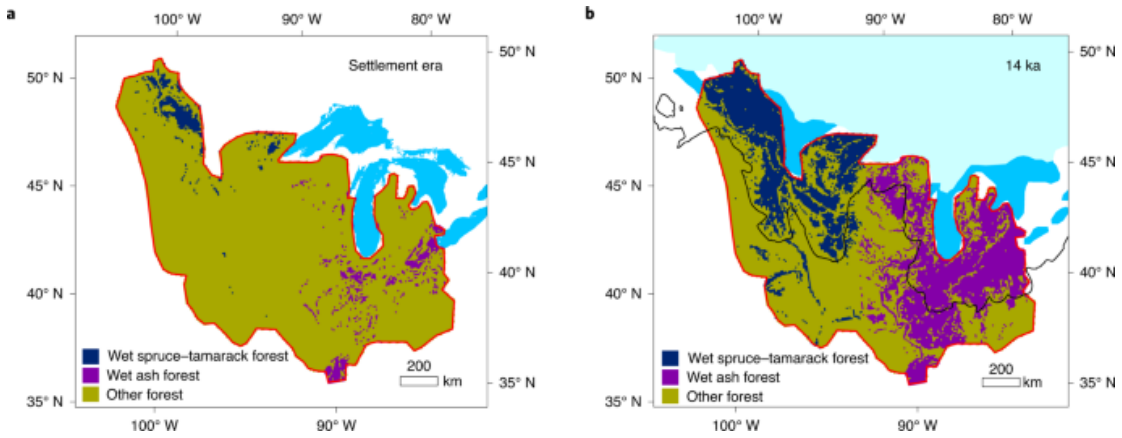

Figure 3. Potential distribution of the two subregional wet forests. a, Early settlement-era, with separation of the two wet forest types. b, 14 ka distributions, with expanded wetlands (50% of the land surface; Methods) and the two wet forest types in close proximity. The black solid line shows the ice-sheet terminal position at the Last Glacial Maximum. The area outlined in red corresponds to the 14 ka parkland biome (Fig. 1).

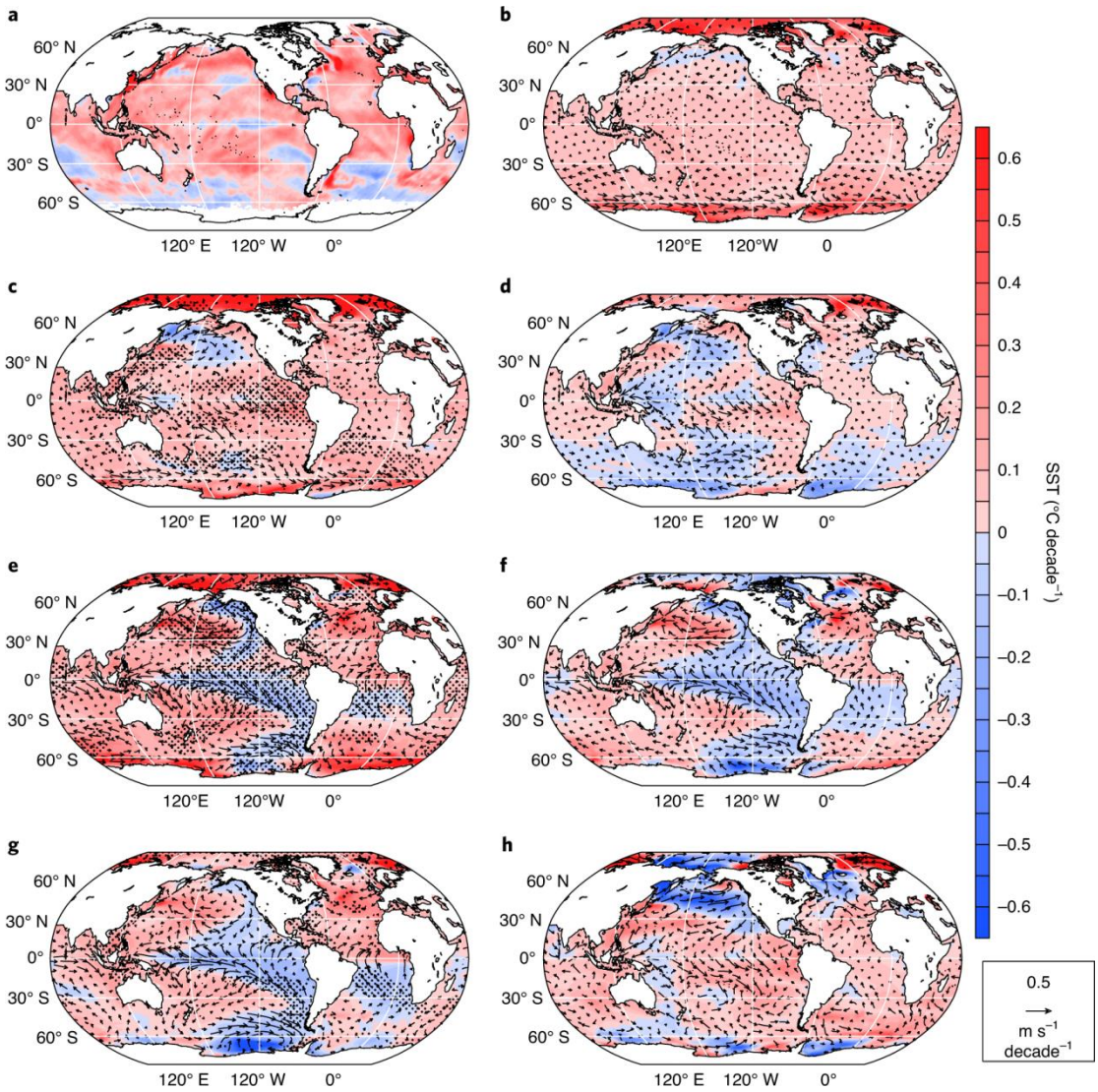

Figure 4. Positive PDV and AMV trending positive to negative. SST trend for the time-series pacemakers (Methods) calculated from 1975 to 2000 for positive PDV and AMV trending from negative to positive. a, Observed SSTs from Hadley Centre Sea Ice and Sea Surface Temperature (HadISST). b, Ensemble average from LENS representing externally forced signal, SST (colours, °C decade−1) and surface winds (vectors, m s−1, scaling arrow at lower right). c, Pacific pacemaker ensemble mean (EM). d, Pacific pacemaker in c minus LENS in b. e, Atlantic pacemaker EM. f, Atlantic pacemaker in e minus LENS in b. g, Atlantic pacemaker EM with aerosols fixed at 1920 values. h, Same as g except for Pacific pacemaker. Stippling in left panels for model pacemaker experiments indicates regions that are significant above the 95% confidence level on the basis of a two-sided t test.

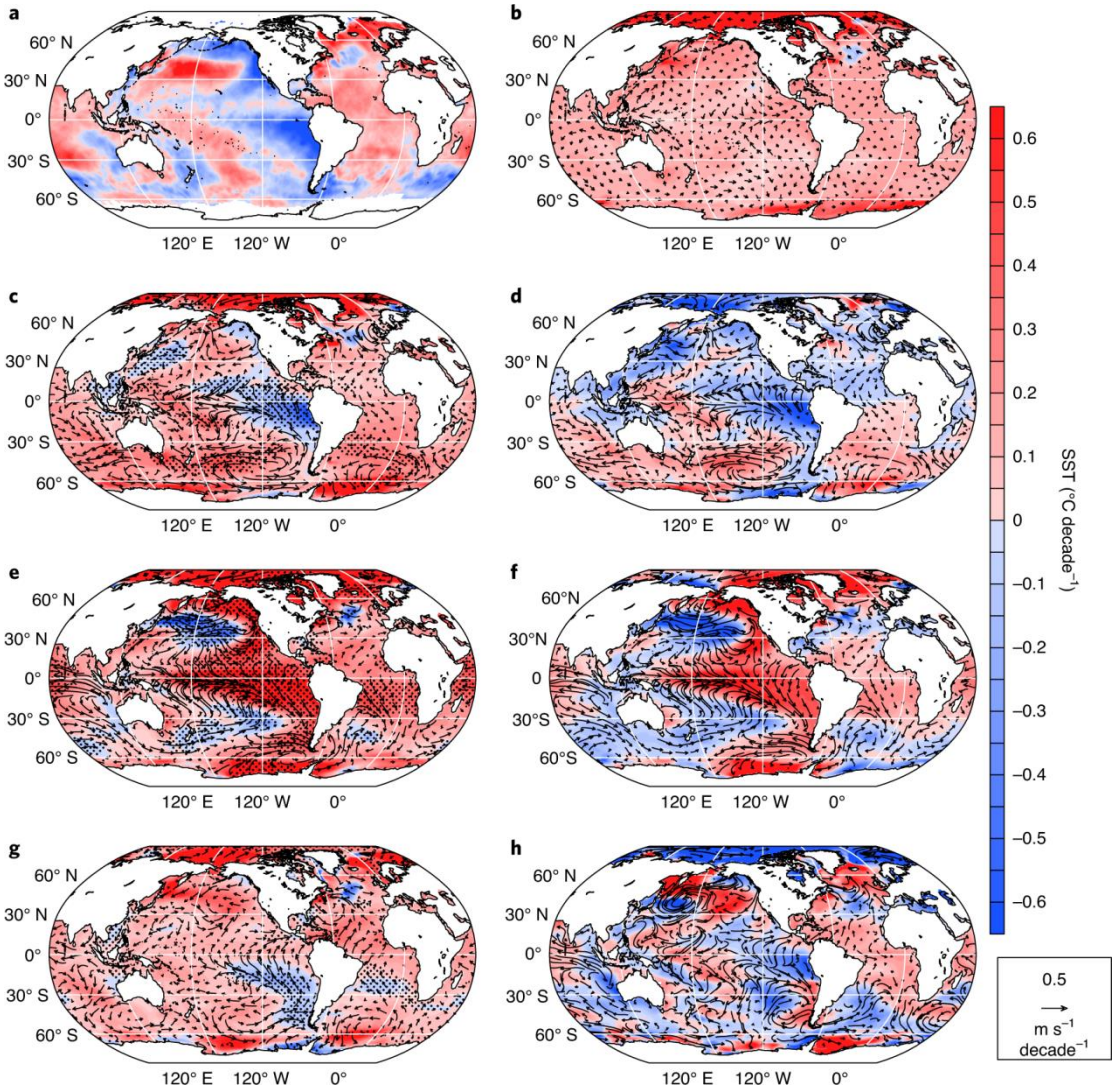

Figure 5. Positive AMV and PDV trending positive to negative. SST trend for the time-series pacemakers (Methods) calculated from 1996 to 2010 for positive AMV and PDV trending from positive to negative. a, Observed SSTs from HadISST. b, Ensemble average from LENS representing externally forced signal, SST (colours, °C decade−1) and surface winds (vectors, m s−1, scaling arrow at lower right). c, Pacific pacemaker EM. d, Pacific pacemaker in c minus LENS in b. e, Atlantic pacemaker EM. f, Atlantic pacemaker in e minus LENS in b. g, Atlantic pacemaker EM with aerosols fixed at 1920 values. h, Same as g except for Pacific pacemaker. Stippling in left panels for model pacemaker experiments indicates regions that are significant above the 95% confidence level on the basis of a two-sided t test.